Contents lists available at ScienceDirect

Geochimica et Cosmochimica Acta

Iron projectile fractionation processes in siliceous glass from small impact craters

Aaron J. Cavosie [a,*], Phil A. Bland [a], Noreen J. Evans [b], Kai Rankenburg [b], Malcolm P. Roberts [c], Luigi Folco [d,e]

[a] Space Science and Technology Centre and The Institute for Geoscience Research, School of Earth and Planetary Science, Curtin University, Perth, WA 6102, Australia
[b] John de Laeter Centre, Curtin University, Perth, WA 6102, Australia
[c] Centre for Microscopy, Characterisation, and Analysis, University of Western Australia, Perth, WA 6009, Australia
[d] Dipartimento di Scienze della Terra, Università di Pisa, Pisa, 56126, Italy
[e] Centro per l'Integrazione della Strumentazione dell'Università di Pisa, Pisa 56126, Italy

ARTICLE INFO

ABSTRACT

Detection of extra-terrestrial geochemical components in melt generated during meteorite impact provides diagnostic evidence that can be used to confirm a hypervelocity impact event, and in some cases, classify the projectile. However, projectile contamination is often present at sub-percent levels, and can be difficult to detect. In contrast, meteoritic abundances in glass from small impact craters (<1 km diameter) formed by iron meteorites can be anomalously high, which has been attributed to glass originating from the projectile-target interface. Emulsion textures, immiscible liquids, metal spherules, and non-meteoritic siderophile element ratios have been cited as evidence that the projectile component is typically fractionated in impact glass. Here we present compositional data for impact glass from the Henbury crater field in Australia, where the largest crater is 145 m in diameter and the subgreywacke target rock and IIIAB iron projectile are geochemically distinct. Mixing models (Fe-Si, Ni-Co, Cr-Ir) and high platinum group element abundances indicate average projectile contributions ranging from 3 to 13 % in Henbury glass, comparable to ranges reported in glass from the Kamil (Egypt) and Wabar (Saudi Arabia) impact craters. However meteoritic siderophile element ratios (Fe:Ni, Fe:Co, Ni:Co) in Henbury glass appear nearly unfractionated, whereas Wabar and Kamil glasses have more fractionated ratios. Observed variations are attributed to fractionation of meteoritic Ni by formation of immiscible Ni-rich spherules during oxidation of meteoritic iron, and subsequent separation of Ni-rich spherules from glass during ejection. The Henbury glass sample analyzed is interpreted as an example of an interface melt that quenched prior to extensive oxidation and phase separation, and thus may represent one of the least fractionated samples of melt from the projectile-target interface described thus far, whereas Wabar and Kamil glasses record more evidence of fractionation processes. These results further highlight the influence of metal spherule formation on the composition of ejected glass from small impact structures formed by iron meteorites and provide new insights that explain textural features observed in natural impact glasses.

1. Introduction

Identification of extra-terrestrial projectile contamination (i.e., a meteoritic component) in terrestrial impactites is one of only a few criteria that can provide unambiguous evidence of hypervelocity impact, and thus can be used to confirm a suspect structure or material as having an impact origin (Alvarez et al., 1980; French and Koeberl, 2010; Osinski et al., 2022). Elevated abundances and elemental ratios of iron, siderophile elements (Ni, Co, Cr), and platinum group elements

(PGE, Os, Ir, Ru, Rh, Pd, Pt) provide a means to detect and quantify the amount of projectile present; isotopic ratios can, in some cases, be used to classify the projectile (Goderis et al., 2013; Koeberl, 2014). The abundance of projectile contamination in most impact melt rocks is often < 1 % (Evans et al., 1993; Koeberl et al., 2012, 2014; Goderis et al., 2013); the highest reported concentrations in impact melt rocks from large impact structures (>1 km) include ~ 5 % from Morokweng, South Africa (Koeberl et al., 1997), 7 % from Zhamanshin, Kazakhstan (Magna et al., 2017), and 8 % from East Clearwater, Canada (Grieve et al., 1980).
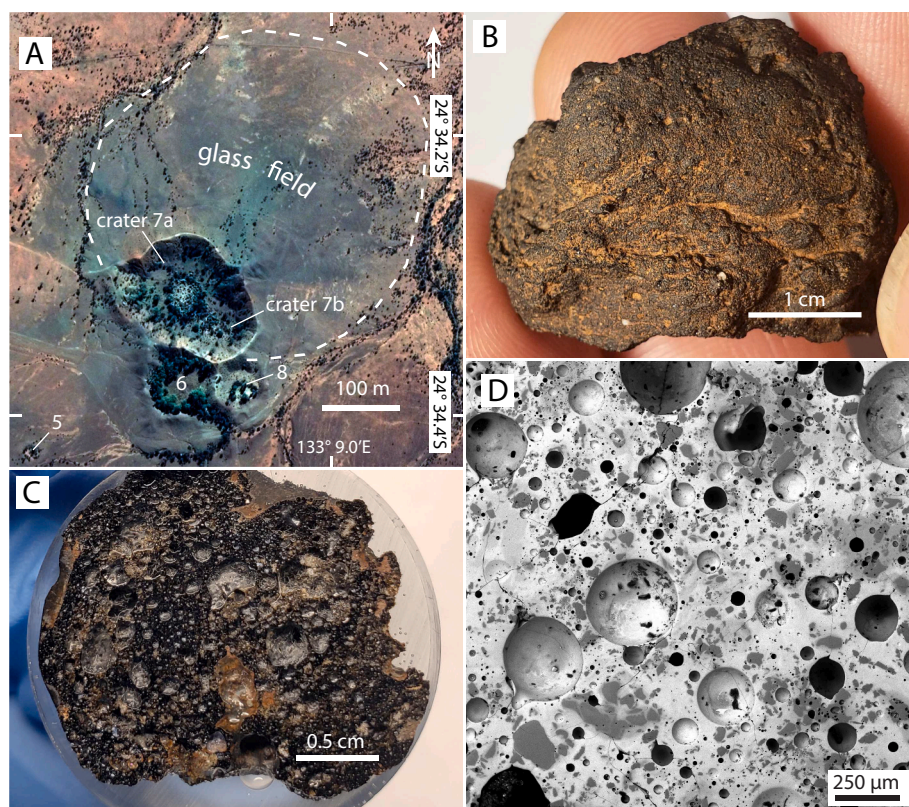

Fig. 1. Images of the Henbury crater field and glassy impactite. (A) Satellite image from Google Earth showing the location of the Henbury impact crater field in Northern Territory, Australia. Labels indicate crater number (not all are shown). (B) Henbury impactite. (C) Polished section of Henbury impact glass. (D) Back-scattered electron (BSE) image of Henbury glass. Intermediate grey objects are mineral inclusions; round features are vesicles.

In contrast, iron-rich silicate glasses from small impact craters (<1 km) formed by collisions of iron meteorites into siliceous target rocks, such as those from Kamil (Egypt) and Wabar (Saudi Arabia), can have projectile abundances ≥ 10 % (e.g., Mittlefehldt et al., 1992; Fazio et al., 2016). The nature of the interaction between melting of iron meteorites and silica-rich target rocks has been studied in both natural samples and experimentally (Hamann et al., 2013; Ebert et al., 2014; Fazio et al., 2016; Hamann et al., 2018). Work on iron-rich silicate impact glasses has demonstrated they are typically heterogeneous in composition at all scales, and that silicate liquid immiscibility and phase separation processes are common (e.g., Ebert et al., 2014; Hamann et al., 2018; Folco et al., 2022).

Here we investigate an impact glass sample (impactite) from the Henbury crater field in Australia. Henbury glass is similar to that found at both Kamil and Wabar craters, in that it is generally a dark coloured, iron-rich silicate glass formed by impact of an iron meteorite into a siliceous target rock. Previous studies have reported compositional data for Henbury glass (Spencer, 1933; Taylor and Kolbe, 1964; Taylor and Kolbe, 1965; Taylor, 1966,1967; Taylor and McLennan, 1979), described mineral inclusions in the glass (Ding and Veblen, 2004), as well as metallic spherules in glass and adjacent soils (Gibbons et al., 1976; Hodge and Wright, 1971). We report new compositional data for Henbury glass using in situ microanalytical methods that allow the quantification of projectile abundance through use of multiple element proxies, and also the first description of shocked minerals from the Henbury crater field. We also compare compositional data for Henbury glass with data for glasses from the Kamil and Wabar craters. The results provide new insights on target-projectile interactions, and highlight the influence of immiscible metal spherule formation on the composition of ejected glass from small impact structures formed by iron meteorites.

2. Materials and Methods

The Henbury crater field is a cluster of at least 13 small and closely spaced impact craters located in Northern Territory, Australia (Alderman, 1932; Spencer, 1933; Milton, 1968; Buhl and McColl, 2015; Quintero et al., 2021). In oral traditions of Aboriginal people from the area the site is called Tatyeye Kepmwere (Hamacher and Goldsmith, 2013). Individual craters at Henbury range from 10 s of meters up to 145 m in diameter. The two largest craters (designated 7a and 7b) form an oval-shape composite crater 180 m across; crater 7a is the largest at 145 m (Fig. 1A). Target rocks at Henbury are part of the Winnall Group, a sequence of Neoproterozoic to Cambrian siliciclastic rocks, including sandstone and shale (Cook, 1968; Normington et al., 2018). Bedrock exposed in crater 7a is subgreywacke, which contains, on average, 36.5 wt% Si, 3.07 wt% Fe, 21 µg/g Ni, and 10 µg/g Co (Taylor and Kolbe, 1964, 1965; Taylor, 1966, 1967; Taylor and McLennan, 1979). The Henbury iron is a IIIAB medium octahedrite (Buchwald, 1975), which contains, on average, 91.95 wt% Fe, 7.43 wt% Ni, and 0.44 wt% Co (e.g., Taylor and Kolbe, 1965; Wasson et al., 1998). Ejected impact glass (i.e., Henbury impactite) is found over a broad area on the north side of the crater field, where it is heterogeneously distributed along rays up to 200–300 m from crater 7a (Fig. 1A; Taylor, 1967).

Henbury glass sample SC0056 was acquired from the U.S. Geological Survey Astrogeology Terrestrial Analog Sample Collection. It was collected by Eugene and Carolyn Shoemaker and described as 'Henbury impactite'. The sampling location is not recorded, but is assumed to have been within the main glass field (Fig. 1A).

The Henbury sample was prepared as a polished 25 mm epoxy mount. Scanning electron microscopy (SEM) was conducted in the John de Laeter Centre (JdLC) at Curtin University using a Tescan Mira3 SEM for backscattered electron (BSE) imaging. Analysis of Henbury glass by electron microprobe analyzer (EMPA) was conducted using a JEOL JXA-

Table 1
EMPA data for Henbury glass sample SC0056 (in wt%).

Oxide DL	SiO_2 0.03	FeO 0.05	Al_2O_3 0.02	K_2O 0.01	MgO 0.02	TiO_2 0.02	CaO 0.02	Na_2O 0.03	MnO 0.06	P_2O_5 0.05	SO_3 0.03	Cr_2O_3 0.02	Total
1–1	55.73	20.58	11.67	2.95	1.89	0.98	0.77	0.62	0.09	0.14	0.03	BDL	95.44
1–2	55.47	20.67	11.53	3.03	1.79	0.81	0.75	0.67	0.23	0.09	0.03	BDL	95.07
1–3	56.56	20.69	11.13	2.94	1.86	0.82	0.54	0.54	0.15	0.11	BDL	BDL	95.35
1–4	55.52	22.45	10.41	2.65	1.80	0.72	0.64	0.63	BDL	0.07	0.03	BDL	94.92
1–5	57.24	21.28	10.70	2.63	1.83	0.76	0.63	0.66	0.13	0.07	0.03	BDL	95.97
1–6	56.58	21.64	10.86	2.88	1.69	0.70	0.68	0.61	0.10	0.14	BDL	0.02	95.92
1–7	57.66	20.74	10.39	2.76	1.70	0.78	0.19	0.56	0.09	0.12	BDL	0.02	95.02
1–8	57.75	21.66	10.57	2.86	1.70	0.74	0.83	0.53	BDL	0.15	0.05	BDL	96.86
1–9	58.69	20.02	11.29	2.89	1.68	0.80	0.89	0.61	0.07	0.12	BDL	BDL	97.09
1–10	57.83	20.42	10.74	2.84	1.76	0.84	0.73	0.53	0.17	0.05	BDL	BDL	95.91
1–11	57.94	20.66	10.86	2.88	1.73	0.90	0.80	0.61	BDL	BDL	BDL	BDL	96.43
1–12	55.99	22.11	11.22	2.81	1.87	0.89	0.44	0.50	0.12	0.06	BDL	BDL	96.03
1–13	58.02	19.65	10.63	2.94	1.74	0.75	0.88	0.61	BDL	0.08	BDL	BDL	95.36
1–14	59.44	19.23	10.27	3.09	1.63	0.76	0.20	0.58	BDL	0.05	0.03	BDL	95.31
1–15	55.80	20.01	12.11	2.95	2.06	0.85	1.17	0.59	BDL	BDL	0.03	0.02	95.67
1–16	56.98	21.75	10.31	2.68	1.77	0.89	0.92	0.62	0.20	0.10	0.03	0.02	96.27
A1 Avg	*57.08*	*20.85*	*10.92*	*2.86*	*1.78*	*0.81*	*0.69*	*0.59*	*–*	*0.10*	*–*	*–*	*95.79*
2–17	62.15	15.25	12.36	3.40	2.05	0.88	0.66	0.74	0.13	0.08	BDL	BDL	97.71
2–18	61.94	15.91	11.33	3.22	1.90	0.84	0.57	0.71	0.07	0.14	BDL	0.02	96.65
2–19	61.27	16.21	12.10	3.22	2.02	0.90	0.42	0.73	0.21	0.10	BDL	BDL	97.18
2–20	61.12	16.16	12.12	3.22	1.91	0.85	0.59	0.72	0.18	0.12	BDL	BDL	96.99
2–21	62.74	14.87	11.94	3.33	1.83	0.87	0.60	0.83	0.28	0.06	BDL	BDL	97.38
2–22	61.31	15.26	12.36	3.36	1.95	0.98	0.65	0.74	0.19	0.07	BDL	BDL	96.88
A2 Avg	*61.76*	*15.61*	*12.03*	*3.29*	*1.94*	*0.89*	*0.58*	*0.74*	*0.18*	*0.09*	*–*	*–*	*97.13*
3–23	61.70	15.21	11.56	3.64	1.69	0.91	0.51	0.88	BDL	0.12	BDL	BDL	96.24
3–24	59.46	18.41	10.62	3.14	1.61	0.85	0.59	0.65	BDL	0.06	BDL	BDL	95.39
3–25	58.06	17.17	12.77	3.23	2.13	0.96	0.60	0.72	BDL	0.05	BDL	BDL	95.73
3–26	59.74	18.29	10.59	3.09	1.77	0.80	0.68	0.73	0.13	0.10	0.03	BDL	95.97
3–27	59.22	15.76	13.09	3.71	2.08	1.01	1.01	0.68	BDL	0.17	BDL	0.02	96.78
A3 Avg	*59.63*	*16.97*	*11.72*	*3.36*	*1.86*	*0.91*	*0.68*	*0.73*	*–*	*0.10*	*–*	*–*	*96.02*
4–28	65.40	13.71	10.90	3.06	1.79	0.83	0.49	0.63	BDL	0.06	BDL	0.02	96.89
4–29	64.41	13.24	11.09	3.21	1.80	0.85	0.41	0.73	0.06	bdl	BDL	BDL	95.85
4–30	64.19	12.91	11.03	3.49	1.77	0.84	0.43	0.71	0.06	0.05	BDL	0.02	95.52
4–31	58.44	18.89	12.34	2.75	2.06	0.88	1.17	0.57	BDL	BDL	BDL	BDL	97.14
4–32	58.80	19.35	12.41	2.73	1.96	0.86	1.24	0.50	BDL	BDL	0.05	BDL	97.97
A4 Avg	*62.25*	*15.62*	*11.55*	*3.05*	*1.87*	*0.85*	*0.75*	*0.63*	*–*	*–*	*–*	*–*	*96.67*
Highest	65.40	22.45	13.09	3.71	2.13	1.01	1.24	0.88	0.28	0.17	0.05	0.02	97.97
Lowest	55.47	12.91	10.27	2.63	1.61	0.70	0.19	0.50	BDL	BDL	BDL	BDL	94.92
Avg	59.16	18.44	11.35	3.05	1.84	0.85	0.68	0.65	–	–	–	–	96.22
2SD	5.49	5.73	1.59	0.56	0.28	0.15	0.50	0.18	–	–	–	–	1.65
2SD (%)	9.3	31	14	18	15	18	74	28	–	–	–	–	1.7

DL = detection limit; BDL = below DL; SD = standard deviation; Spot size = 10 μm.
A1-4 = areas 1–4; Avg = average.

8530F field emission microscope with Probe for EMPA acquisition software at the Centre for Microscopy, Characterization and Analysis at the University of Western Australia. Operating conditions included a 15 kV accelerating voltage, 15nA current, and a 10 μm defocused beam. Twelve elements (Si, Al, Fe, Ti, K, Na, Ca, Mg, Mn, Cr, P, S) were analyzed, with spots clustered in four randomly chosen different areas within the 2-cm sample (Table 1, areas 1–4). A combination of glass and mineral standards were used; Smithsonian Institution basaltic glass (NMNH111240-52 VG2) was analyzed to estimate precision (Jarosewich et al., 1980). Calculated error based on nine analyses of VG-2 glass are 0.1 rel% (Ti), 1–3 rel% (Si, Ca, Mg, Mn, Na, Fe), and 6–8 rel% (Al, K, P). All abundances measured in Henbury glass by EMPA are above 3x the detection limit, except for Mn, P, S, and Cr.

Analysis of Henbury glass by laser ablation-inductively coupled plasma-mass spectrometry (LA-ICP-MS) was done using a RESolution-SE incorporating a COMPex 102 excimer laser, coupled to an Agilent 8900 QQQ ICP-MS at the GeoHistory Facility, JdLC, Curtin University. Data reduction used the Trace Elements data reduction scheme in Iolite 3 or Iolite 4 (Paton et al., 2011). Henbury glass was analyzed in three different sessions, each using ^{29}Si as the internal standard element with an EMPA-determined Si content of 27.5 wt% Si (Table 1). The first LA-ICP-MS session included analysis of 37 elements including major, minor, and trace elements (Table 2). In session 1 glass standard NIST 612 was used as the primary reference material to calculate elemental concentrations and correct for drift. After two cleaning pulses and 30 s baseline acquisition, samples and standards were ablated for 35 s using a 50 μm spot at 5 Hz and 2 J cm^{-2}. Secondary reference glasses ATHOG, BCR-2G and GSD-1G (Jochum et al., 2005; GEOREM preferred values; https://georem.mpch-mainz.gwdg.de/) were analyzed in blocks throughout the run (n = 10) with recommended values reproduced to within 5 %. All abundances measured in Henbury glass during session 1 are above 3x the detection limit.

The second LA-ICP-MS session focused on siderophile and PGE and involved analysis of 10 elements (S, Cr, Fe, Co, Ni, Cu, Mo, Rh, Ir, Pt), including multiple isotopes for Ni, Cu, and Pt to evaluate the effect of unanticipated interferences (none detected) (Table 3). In session 2 glass standard NIST 610 was the primary reference material for most elements, with GSD-1G used for Ir (nominal 12 μg/g; Jochum et al., 2005). After two cleaning pulses and 60 s baseline acquisition, samples and standards were ablated for 30 s using a 80 μm spot at 10 Hz and 2.5 J cm^{-2}. Secondary standards NIST 612, ATHOG and GSE-1G (Jochum et al., 2005) were analyzed in blocks throughout the run (n = 21). NIST 612 reproduced recommended values for Cr, Rh and Pt to 5 %, 1.7 % and 14 %; no reliable Ir values are given for the common silicate glass standards used, so accuracy is difficult to determine. In a separate analytical session (results not reported here), data for sample SC0056

Table 2

LA-ICP-MS data (Session 1) for Henbury glass sample SC0056 (in μg/g).

Spo	Mass	DL	1-1	1-2	1-3	1-4	1-5	1-6	1-6	1-8	1-9	1-10	2-11	2-12	2-13	2-14	2-15	3-16	3-17	3-18	3-19	3-20	4-21	4-22	4-23	4-24	4-25	Avg	2SD	2SD (%)
Li	7	0.05	37.4	41.6	40.4	42.2	40.8	41.0	44.4	42.7	42.1	45.7	51.2	45.5	48.2	47.8	46.3	44.3	44.8	45.1	45.5	50.4	36.0	37.5	41.2	41.6	37.2	43.2	8.0	18
B	11	0.4	56.1	72	58.9	63.4	59.4	70.9	54.1	52.2	63.1	63.7	80	73.9	74.4	78.1	75.3	57.2	54.1	62	62.9	85.70	36.2	58.70	57.6	54.5	33.8	62.3	24.6	40
Na	23	0.8	4050	4180	4330	4450	4280	4320	4450	4390	4360	4500	5340	4820	4970	4920	4740	5190	4590	4790	4700	5520	3750	4220	4620	4510	3870	4550	850	19
Mg	25	0.2	11300	13600	11300	11850	11600	11500	11700	11800	11300	12400	12100	11100	11500	11500	11650	10600	11900	10200	10700	11400	11700	12100	11300	10900	12800	11600	1400	12
Al	27	0.2	59700	65900	60080	63690	61190	62200	62030	63500	61830	64840	65690	60000	62220	63300	62060	57080	60140	57500	59890	64240	62900	61880	57810	56430	68370	61800	5825	9
K	39	1	23500	26300	23300	24400	23500	23800	23600	23900	23500	23900	26900	25200	25350	26100	25300	23800	23600	24900	24300	28500	21500	22500	23900	23500	21900	24300	3090	13
Ca	43	40	5090	8540	5490	5920	5290	5250	5670	6280	4970	5350	3490	3060	3840	3730	3590	3770	5160	3340	3730	3170	7210	3500	2630	2600	8510	4770	3310	69
Sc	45	0.04	11.7	13.0	11.8	12.7	12.2	12.3	12.4	12.9	12.3	12.8	12.9	11.9	12.1	12.2	12.3	12.4	12.4	11.9	13.2	12.8	12.3	11.4	11.0	13.8	12.3	1.3	11
Ti	47	0.1	4860	5870	4985	5090	5100	5150	5280	5320	5090	5220	5360	4820	5210	5310	5160	4800	5070	4770	4920	5385	5020	5550	5580	4870	5560	5170	555	11
V	51	0.02	82.5	93.6	83.9	90.2	85.9	86.1	87.6	91.4	85.9	92.7	92.1	85.3	87.3	88.6	88.0	79.8	84.5	80.3	83.7	85.9	77.9	83.9	77.2	75.9	84.5	85.4	9.5	11
Cr	52	0.2	94.0	94.4	89.9	93.4	95.8	94.3	96.6	97.6	94.0	98.6	78.2	78.4	81.7	80.6	84.3	86.7	85.6	78.2	85.3	74.1	71.5	75.6	75.6	69.1	77.5	85.2	18.2	21
Mn	55	0.3	797	1040	790	809	761	760	789	737	741	1110	1030	843	827	778	765	774	1020	808	766	759	721	817	737	696	776	818	219	27
Fe	57	2	162000	147300	144000	137500	164500	164900	165600	163200	162400	162600	105500	106800	115700	116000	120760	145000	130900	120700	139000	95900	137000	104200	100140	96000	157300	134600	49400	37
Co	59	0.01	672	556	580	539	690	726	667	673	680	676	374	383	428	424	458	592	505	477	561	329	456	348	334	526	520	258	50
Ni	60	0.06	9920	7850	8425	7980	10400	11300	9850	10400	9980	10200	5880	6100	6920	7010	7560	9670	8170	7780	9420	5430	5280	4620	5260	4970	6150	7860	4060	52
Cu	63	0.02	28.3	29.7	28.10	27.1	29.6	30.4	30.9	29.9	30.2	32.3	31.4	30.2	32.6	31.6	31.7	34.0	31.3	32.1	33.1	31.3	20.3	22.2	22.5	23.6	21.7	29.0	7.8	27
Zn	66	0.08	26.1	56.6	31.80	36.0	28.1	25.0	23.3	22.1	24.6	30.3	46.3	43.5	42.7	38.0	25.3	29.8	33.1	24.2	41.4	26.9	40.3	39.4	38.7	27.3	33.7	17.8	53
Rb	85	0.02	125	137	123	130	126	128	125	129	125	129	146	136	138	141	139	128	128	135	132	152	110	120	124	124	113	130	18.9	15
Sr	88	0.01	86.8	102	89.0	95.3	89.4	87.8	91.5	93.9	89.9	93.4	95.1	87.0	90.8	92.2	90.2	82.8	89.0	83.5	93.5	90.80	97.5	79.8	78.8	75.6	106	90.1	13.6	15
Y	89	0.001	30.3	41.0	29.10	30.3	29.5	29.0	28.8	27.7	30.0	29.0	31.7	28.9	30.7	30.0	29.9	28.9	32.5	29.4	29.0	40.8	28.8	27.8	28.9	26.5	39.0	30.7	7.6	25
Zr	91	0.02	251	318	258	263	262	274	267	233	271	253	279	260	294	267	274	267	302	260	281	623.0	249	240	271	252	264	281	147	52
Nb	93	0.001	13.3	15.5	13.5	13.7	14.2	14.2	14.5	14.4	13.8	14.8	15.1	13.8	14.7	14.7	14.4	13.1	13.9	13.2	13.4	14.8	13.3	14.6	14.8	12.9	14.4	14.1	1.4	10
Ba	137	0.01	371	435	431	467	393	370	403	383	383	396	400	407	380	395	376	356	365	382	365	408	418	395	314	309	457	390	72.9	19
La	139	0.001	45.0	42.8	37.6	38.5	37.1	36.2	36.9	35.3	37.1	39.0	41.5	35.9	37.6	37.7	39.0	35.2	36.2	33.9	38.3	37.7	36.2	34.9	35.1	32.8	38.8	37.5	5.4	14
Ce	140	0.001	93.9	90.0	78.3	81.7	78.3	76.1	76.9	73.2	76.3	84.5	88.4	75.9	80.5	83.4	89.7	74.2	76.2	71.6	80.2	79.5	74.5	70.5	74.3	70.8	79.4	79.1	12.5	16
Pr	141	0.001	10.4	10.1	8.88	9.24	8.68	8.52	8.57	8.18	8.53	9.13	9.74	8.50	8.69	8.77	9.09	8.19	8.54	7.91	8.95	8.79	8.29	8.08	8.16	7.74	9.07	8.75	1.3	15
Nd	146	0.005	39.2	38.1	32.9	34.9	32.9	31.5	32.0	31.0	32.3	34.2	36.5	32.0	32.7	32.8	34.3	30.9	31.6	29.3	33.5	33.0	31.2	30.5	30.8	29.0	34.2	32.9	4.9	15
Sm	147	0.01	7.66	7.92	6.86	7.09	6.79	6.51	6.56	6.10	6.62	6.75	7.34	6.41	6.60	6.57	6.41	6.43	5.90	6.80	6.96	6.22	6.09	6.22	6.12	7.09	6.66	1.0	15
Eu	153	0.002	1.35	1.43	1.20	1.30	1.18	1.16	1.25	1.20	1.21	1.20	1.37	1.20	1.21	1.25	1.28	1.18	1.22	1.15	1.22	1.31	1.17	1.15	1.18	1.12	1.33	1.23	0.2	13
Gd	157	0.01	6.21	7.12	5.61	6.36	5.75	5.51	5.59	5.38	5.96	5.79	6.21	5.72	6.05	5.66	5.96	5.41	5.92	5.37	5.50	6.71	5.52	5.29	5.76	5.20	6.06	5.82	0.9	16
Dy	163	0.003	5.74	7.53	5.56	5.50	5.45	5.35	5.19	5.05	5.53	5.47	5.78	5.41	5.77	5.74	5.60	5.28	6.02	5.45	5.30	7.33	5.27	5.18	5.20	4.85	6.82	5.65	1.3	23
Er	166	0.002	3.11	4.35	3.01	3.22	3.05	3.10	3.18	2.95	3.21	3.06	3.38	3.13	3.29	3.23	3.26	3.04	3.35	3.10	3.06	4.63	3.08	2.99	3.06	2.86	4.31	3.28	0.9	28
Yb	173	0.01	2.94	4.32	3.01	2.93	2.98	3.10	3.02	2.91	3.12	3.11	3.22	3.01	3.42	2.98	3.13	3.00	3.31	2.81	3.03	4.52	3.14	2.96	2.77	2.78	4.39	3.20	1.0	30
Hf	178	0.003	6.74	8.31	7.08	7.23	6.99	7.27	7.14	6.38	7.38	6.91	7.82	7.15	8.00	7.20	7.51	7.25	8.16	7.39	7.52	16.90	6.99	6.24	7.03	6.68	7.16	7.62	4.0	52
Pb	208	0.01	7.21	11.8	8.16	8.99	7.19	6.43	5.91	5.14	6.00	7.17	11.4	10.6	10.1	10.0	9.42	6.88	7.24	9.94	6.69	11.6	6.45	9.69	9.62	9.61	6.36	8.38	4.0	47
Th	232	0.001	16.5	17.8	16.0	16.7	16.1	16.2	15.7	15.6	16.4	16.2	17.8	15.6	16.4	16.3	16.7	15.1	17.1	15.2	15.7	18.2	15.7	16.2	15.8	14.4	16.6	16.2	1.7	11
U	238	0.001	3.60	4.11	3.49	3.71	3.52	3.55	3.56	3.54	3.56	3.63	4.08	3.85	3.99	3.92	3.60	3.85	3.71	3.75	4.65	2.73	3.32	3.89	3.28	3.05	3.67	0.7	20
Fe:Ni			16.3	18.8	17.1	17.2	15.8	14.6	16.8	15.7	16.3	15.9	17.9	17.5	16.7	16.5	16.0	15.0	16.0	15.5	14.8	17.7	25.9	22.6	19.0	19.3	25.6	17.6	6.0	34
Ni:Co			23.7	18.7	20.6	19.9	23.3	23.9	21.6	22.5	22.5	20.9	11.9	12.7	13.1	13.4	14.4	17.4	16.1	14.9	16.9	10.5	22.5	15.7	15.5	14.2	24.2	18.0	8.6	48

DL = detection limit; SD = standard deviation; Spot size = 50 μm diameter.

DL = detection limit; SD = standard deviation; Spot size = 50 μm diameter.

were calibrated against a non-matrix matched PGE-rich pyrrhotite reference material (LaFlamme Po726) and yielded values within 14 % of the average Ir value for sample SC0056 in Table 3; Pt values from this additional session yielded an average value within 5.3 % of that generated using the GSD-1G glass standard, providing additional confidence in the accuracy of Pt data for sample SC0056 in Table 3. All abundances measured in Henbury glass during session 2 are above 3x the detection limit.

The third LA-ICP-MS session focused primarily on PGE. Session 3 involved analysis of 7 elements (Ru, Rh, Pd, Re, Os, Ir, Pt), including multiple isotopes for Ru, Pd, Os, Ir, and Pt to evaluate the effect of unanticipated interferences (none detected) (Table 4). Glass standard IZ01 was used as the primary reference material in session 3. The standard IZ01 is a basaltic glass doped with PGE in concentrations ranging from 10 s to 1000 s of μg/g that has been shown to be homogeneous in composition and thus ideal for LA-ICP-MS calibration (Chen et al., 2020). After two cleaning pulses and 35 s baseline acquisition, samples and standards were ablated for 30 s using a 100 μm spot (samples) and 50 μm spot (standards) at 10 Hz and 2.5 J cm^{-2}. Secondary standards NIST 612, StHs6, TiG, BHVO2, and KL2 (Jochum et al., 2005) were analyzed in blocks throughout the run (n = 50). NIST 612 (n = 10) yielded elemental abundances for [103]Rh, [105]Pd, [108]Pd, [185]Re, [191]Ir, [194]Pt, and [195]Pt that are all within < 1 % of recommended values; [193]Ir yielded an abundance within 2.5 % of the recommended value. All abundances measured in Henbury glass during session 3 are above 3x the detection limit, except for Re and Os, for which some analyses were below the detection limit.

New data for dark glass from Kamil crater are also presented. The data include major and trace element concentrations determined by EMPA and LA-ICP-MS (Tables 5 and 6) from six glass spherules. They are from the magnetic fraction of a soil sample collected about 100 m SE of the rim of Kamil crater (22°01′02″N, 26°05′15″E; sample S24 in Folco et al., 2015). The spherules are 300 to 600 μm in diameter, shiny and black, show significant vesicularity, and contain mineral and lithic inclusions. Inclusions mainly consist of bedrock fragments (quartzarenite), silica glass (or lechatelierite), and Fe-Ni oxide and microscopic metal blebs. The heterogeneity of the glass is emphasized by microscopic schlieren and haloes with variable Si/Fe ratios around inclusions in BSE images.

The EMPA used for Kamil glass was the Cameca SX50 electron microprobe at IGG-CNR, Padua, Italy. Operating conditions included a 15 kV accelerating voltage, 15nA beam current, and a 5 μm defocused beam. Multiple spot analyses were made on each particle. The manufacturer-supplied PAP procedure (Pouchou and Pichoir, 1991) was employed for raw data reduction. Standards used include natural minerals (quartz, diopside, olivine) and pure elements (Fe, Ni, and Co). Detection limits (element wt%) are 0.04 for Si and Al, and 0.05 for Fe, Ni and Co (Table 5).

Analysis of Kamil glass for Ni and Co by LA-ICP-MS was done using a PerkinElmer SCIEX ELAN DCR-e quadrupole ICP-MS coupled with a UP213 deep-UV YAG Laser Ablation System, New Wave Research, Inc., emitting a laser beam with 213 nm wavelength, at IGG-CNR, Unità Operativa di Pavia. Signals were acquired in peak hopping mode with a 10 ms dwell time. After a 60 s baseline acquisition, samples and standards were ablated for 60 s using a 50 μm spot at 10 Hz, 50 μm spot, and 2.5 mW. Data reduction was performed with the software package Glitter (van Achterbergh et al., 2001). NIST SRM 612 (Pearce et al., 1997) and [29]Si were adopted as external and internal standards, respectively. Precision and accuracy were assessed via repeated analysis of USGS standard BCR-2G (https://minerals.cr.usgs.gov/geochem/basaltbcr2.html, and Gao et al., 2002). Mean detection limits (in μg/g) for Ni and Co are 0.17 and 0.04, respectively (Table 6).

Table 3
LA-ICP-MS data (Session 2) for Henbury glass sample SC0056 (in µg/g).

Element	S	Cr	Fe	Co	Ni	Ni	Cu	Cu	Mo	Rh	Ir	Pt	Pt	Fe:Ni	Ni:Co
Mass	34	52	57	59	60	61	63	65	95	103	193	194	195	57:60	60:59
DL	20	0.19	0.9	0.005	0.06	0.15	0.006	0.007	0.003	0.0003	0.002	0.003	0.003		
1–1	100	90.0	150,000	599	8690	8170	30.6	31.9	0.355	0.127	1.16	0.586	0.662	17.3	14.5
1–2	114	72.2	114,000	479	7690	7250	25.8	27.3	0.413	0.101	1.92	0.603	0.697	14.8	16.1
1–3	169	92.4	152,000	647	10,100	9470	31.2	33.0	0.545	0.138	2.14	0.943	1.01	15.0	15.6
1–4	164	94.5	157,000	676	10,500	9890	31.4	33.0	0.625	0.147	2.58	1.02	1.13	15.0	15.5
1–5	130	75.2	105,000	407	6400	6050	27.5	28.8	0.466	0.0862	1.51	0.642	0.688	16.4	15.7
1–6	101	97.6	151,000	603	8930	8410	31.3	32.9	0.433	0.179	2.09	1.22	1.36	16.9	14.8
1–7	96.0	86.2	134,000	514	7390	6980	26.1	27.3	0.325	0.113	1.18	0.666	0.737	18.1	14.4
1–8	144	79.8	130,000	525	7940	7470	25.4	26.7	0.377	0.136	1.53	0.689	0.794	16.4	15.1
1–9	95.5	61.0	99,900	390	5430	5130	19.9	21.1	0.237	0.0646	0.714	0.367	0.409	18.4	13.9
1–10	121	95.5	158,000	652	9760	9240	30.2	31.5	0.461	0.144	2.02	0.909	0.962	16.2	15.0
A1 Avg	*123*	*84.5*	*135,000*	*549*	*8280*	*7800*	*27.9*	*29.4*	*0.424*	*0.124*	*1.68*	*0.765*	*0.845*	*16.4*	*15.1*
2–11	109	78.7	108,000	420	6940	6560	32.6	34.4	0.466	0.141	1.97	0.890	1.03	15.6	16.5
2–12	98.0	83.4	109,800	415	6850	6470	34.0	35.8	0.444	0.112	1.46	0.720	0.720	16.0	16.5
2–13	80.1	75.5	104,000	403	6580	6240	31.1	32.5	0.445	0.0934	1.30	0.573	0.651	15.8	16.3
2–14	96.2	71.4	98,500	374	6200	5870	30.5	31.8	0.513	0.224	3.97	1.77	1.95	15.9	16.6
2–15	94.0	82.0	111,000	427	7070	6710	33.2	35.0	0.457	0.187	2.23	1.22	1.38	15.7	16.5
A2 Avg	*95.5*	*78.2*	*106,000*	*408*	*6730*	*6370*	*32.2*	*33.9*	*0.465*	*0.151*	*2.19*	*1.03*	*1.15*	*15.8*	*16.5*
3–16	96.6	75.7	114,000	464	7580	7200	31.9	33.3	0.450	0.0904	1.28	0.617	0.702	15.0	16.4
3–17	104	76.2	112,000	464	7510	7100	31.1	32.6	0.486	0.0950	1.24	0.570	0.599	14.9	16.2
3–18	96.0	42.6	64,100	256	4180	3970	19.9	20.8	0.283	0.0491	0.620	0.268	0.279	15.3	16.3
3–19	92.9	81.8	122,000	507	8460	8030	29.5	31.0	0.467	0.175	2.67	1.30	1.46	14.4	16.7
3–20	102	54.1	78,000	313	5230	4990	24.6	26.0	0.365	0.0546	0.619	0.302	0.345	14.9	16.7
3–21	111	76.2	110,000	446	7510	7180	31.4	32.7	0.350	0.139	2.18	0.981	1.08	14.6	16.8
3–22	115	82.7	113,000	409	6800	6490	37.4	39.0	0.416	0.104	1.03	0.571	0.688	16.6	16.6
A3 Avg	*102*	*69.9*	*102,000*	*408*	*6750*	*6420*	*29.4*	*30.8*	*0.402*	*0.101*	*1.38*	*0.658*	*0.736*	*15.1*	*16.5*
4–23	86.0	61.6	86,900	278	3510	3370	18.1	18.9	0.184	0.0372	0.227	0.196	0.204	24.8	12.6
4–24	85.2	72.1	93,500	323	4930	4710	24.5	25.7	0.306	0.110	0.505	0.440	0.477	19.0	15.3
4–25	85.0	68.6	93,600	348	5070	4840	23.1	24.2	0.306	0.0695	0.622	0.485	0.539	18.5	14.6
4–26	77.0	65.4	85,900	314	4670	4470	23.7	24.9	0.287	0.0777	0.603	0.444	0.493	18.4	14.9
4–27	84.2	62.5	83,300	303	4570	4370	23.0	24.0	0.273	0.0759	0.536	0.421	0.436	18.2	15.1
4–28	87.0	69.4	95,200	362	5380	5160	25.1	26.5	0.310	0.0814	0.633	0.532	0.561	17.7	14.9
A4 Avg	*84.1*	*66.6*	*89,700*	*321*	*4690*	*4500*	*22.9*	*24.0*	*0.278*	*0.0752*	*0.521*	*0.420*	*0.452*	*19.4*	*14.6*
Average	105	75.9	112,000	440	6850	6490	28.0	29.4	0.394	0.113	1.45	0.712	0.787	16.6	15.6
2SD	48	26	49,600	233	3630	3380	10.0	10	0.20	0.09	1.70	0.71	0.80	4.20	2.07
2SD (%)	46	34	44	53	53	52	36	33	51	76	117	100	102	25	13

DL = detection limit; SD = Standard deviation; Spot size = 80 µm diameter. A1-4 = areas 1–4. Avg = average.

3. Results

3.1. General Observations of Henbury Glass

The exterior surface of the sample is oxidized to an orange-brown color (Fig. 1B), whereas the interior is black and appears fresh (Fig. 1C). No evidence of alteration was observed, aside from discoloration adjacent to some vesicles. A high density of vesicles is visible on the polished surface (Fig. 1D). In BSE images, the glass is heterogeneous at all scales (Fig. 1D); it contains many inclusions of unmelted to variably melted mineral fragments (mostly quartz and lechatelierite), and also some quartz-rich lithic clasts. High-contrast BSE images reveal that some fractured quartz grains contain multiple orientations of planar deformation features (PDF) (Fig. 2A); orientations were not indexed in this study. Round metal spherules (FeNi, FeNiS, and NiS) are locally present; they are small (up to ~ 10 µm diameter) and not abundant (Fig. 2B-D); only three were observed. An emulsion texture ~ 5 µm across occurs adjacent to one of the metal spherules (e.g., Fig. 2C); no other emulsions were observed. A glass spherule was found accreted to the external surface of the sample (Fig. 2E). The spherule is deformed and locally concave along the contact with the impactite. Vesicles occur in both materials, and the presence of vesicles that cross-cut the spherule-impactite boundary provide evidence that both objects were molten during accretion (Fig. 2E, arrow).

3.2. Composition of Henbury Glass

A total of 32 spot analyses by EMPA for major and minor elements were made in four areas of the Henbury glass sample (Table 1). Average values from the four areas provide evidence of compositional heterogeneity across the 2-cm sample; the two standard deviation (2SD) variation about the mean for all elements but Si is 15–20 %, and > 30 % for Fe and Ca (Table 1). Values for SiO_2 range from 55.5 to 65.4 wt% (avg SiO_2 = 59.2 wt%) and identify the glass as broadly having an intermediate composition. On Harker diagrams (Fig. 3) the elements Al, K, Na, Mg, and Ti show no correlation with Si (R^2 values from 0.01 to 0.47). In contrast, Fe is highly correlated with Si (R^2 = 0.91) over a large range (12.9 to 22.5 wt% FeO). The Henbury glass analyses show considerable to full overlap with published values for the Henbury target subgreywacke (except for Fe and Si), and effectively no overlap with the target quartzite (Taylor and McLennan, 1979).

The Henbury sample was evaluated as a volcanic rock using both the total alkalis vs. silica (TAS) diagram (LeBas et al., 1986), and also the alkali-FeO-MgO (AFM) diagram (Irvine and Baragar, 1971) (Fig. 4). On the TAS diagram Henbury glass ranges from andesite to dacite (Fig. 4A), whereas the target subgreywacke has a composition equivalent to rhyolite, with a comparable total alkali content as Henbury glass. On the AFM diagram Henbury glass plots as ferroan tholeiitic basaltic andesite, whereas the target subgreywacke plots near andesite; the glass falls on an apparent mixing line between the target subgreywacke and the Henbury iron (Fig. 4B).

A total of 25 spot analyses in LA-ICP-MS session 1 were made for major, minor, and trace elements over the same four areas of the Henbury glass sample measured by EMPA (Table 2). Average values determined by LA-ICP-MS agree well with those determined by EMPA despite the difference in size of the analytical volume. The compositional

Table 4
LA-ICP-MS data (Session 3) for Henbury glass sample SC0056 (in µg/g).

Element mass DL	Ru 101 0.002	Ru 102 0.002	Rh 103 0.001	Pd 105 0.004	Pd 108 0.006	Re 185 0.002	Os 189 0.0003	Os 190 0.0002	Os 192 0.0001	Ir 191 0.003	Ir 193 0.002	Pt 194 0.008	Pt 195 0.008
1–1	0.193	0.212	0.0404	0.141	0.152	0.0155	0.00892	0.00829	0.00717	0.221	0.233	0.418	0.422
1–2	0.484	0.494	0.0538	0.101	0.136	0.00792	0.0128	0.0123	0.00931	0.597	0.643	1.03	0.964
1–3	0.275	0.279	0.0414	0.0975	0.101	0.00647	0.00305	0.00342	0.00307	0.293	0.309	0.654	0.704
1–4	0.172	0.148	0.0441	0.0984	0.0882	BDL	0.00367	0.00421	0.00338	0.233	0.250	0.514	0.471
1–5	0.0852	0.0896	0.0131	0.0400	0.0429	BDL	BDL	0.000476	0.000387	0.0568	0.0597	0.150	0.137
1–6	0.183	0.181	0.0259	0.0812	0.0888	BDL	0.000873	0.000781	0.000953	0.290	0.279	0.444	0.414
1–7	0.176	0.182	0.0467	0.112	0.114	BDL	0.00772	0.00787	0.00576	0.389	0.368	0.623	0.810
1–8	0.255	0.232	0.0338	0.0617	0.0878	BDL	0.00656	0.00627	0.00525	0.360	0.371	0.631	0.591
1–9	0.135	0.147	0.0354	0.100	0.125	BDL	0.00133	0.00159	0.00159	0.164	0.175	0.444	0.438
1–10	0.0619	0.0688	0.0134	0.0480	0.0763	BDL	0.00105	0.00105	0.000755	0.117	0.118	0.158	0.166
1–11	0.187	0.181	0.0263	0.0534	0.0737	0.00587	0.00441	0.00494	0.00485	0.311	0.307	0.491	0.480
1–12	0.223	0.234	0.0282	0.0722	0.0825	0.00737	0.00655	0.00662	0.00599	0.351	0.365	0.484	0.494
1–13	0.404	0.454	0.0460	0.0840	0.0906	0.0134	0.0159	0.0185	0.0163	0.608	0.636	1.13	1.58
1–14	0.398	0.391	0.0456	0.0736	0.0906	0.0116	0.00852	0.00793	0.00687	0.471	0.489	0.777	0.716
1–15	0.373	0.502	0.0449	0.0715	0.0750	0.00673	0.0185	0.0294	0.0134	0.764	0.614	1.70	0.928
1–15 s	1.93	1.90	0.122	0.0638	0.114	BDL	0.148	0.150	0.118	3.61	3.42	8.03	7.60
1–16	1.46	1.45	0.0713	0.101	0.119	0.00634	0.0723	0.0758	0.0618	2.08	2.09	4.16	4.22
1–16 s	2.57	2.52	0.105	0.0977	0.109	0.00759	0.145	0.149	0.121	3.90	3.84	7.55	7.81
1–17	0.362	0.378	0.0499	0.193	0.686	0.00585	0.0138	0.0158	0.0121	0.540	0.565	1.11	1.00
1–18	0.0723	0.0932	0.0273	0.0917	0.0877	BDL	0.000871	0.000838	0.000894	0.0951	0.111	0.306	0.313
1–19	0.265	0.267	0.0297	0.0671	0.0565	0.00376	0.00565	0.00454	0.00370	0.351	0.341	0.567	0.598
1–20	0.322	0.336	0.0533	0.0861	0.0865	0.00808	0.0123	0.0111	0.00971	0.573	0.592	0.792	0.812
AVG	0.304	0.316	0.0385	0.0888	0.123	0.00824	0.0108	0.0111	0.00866	0.444	0.446	0.829	0.813
2SD	0.59	0.59	0.03	0.07	0.27	0.01	0.03	0.03	0.03	0.86	0.85	1.73	1.74
2SD (%)	195	188	74	77	220	84	293	304	307	194	191	209	213

DL = detection limit; BDL = below detection limit; SD = standard deviation; Spot size = 100 µm. All spots are in area 1.
Average values do not include spots 1-15_s and 1-16_s, which are sub-sets of spots 15 and 16.

heterogeneity measured by LA-ICP-MS (magnitude of variation about mean values) closely mirrors that determined by EMPA (10–20 % for Al, Mg, K, Ti, Na and > 30 % for Fe, Ca). In terms of siderophile elements, the range of Fe values measured by LA-ICP-MS (9.6 to 16.6 wt% Fe) agrees with that determined by EMPA (10.0 to 17.5 wt% Fe). The LA-ICP-MS values for Ni range from 4600 to 11300 µg/g (avg = 7860 ± 4060 µg/g, 2SD), and values for Co range from 330 to 690 µg/g (avg = 520 ± 260 µg/g, 2SD).

When normalized to upper continental crust (UCC, Taylor and McLennan, 1995), Henbury glass shows conspicuous enrichment in Co (>40x) and Ni (>200x), lesser enrichments in other elements (2-5x: Fe, Cr, Zr, Hf, and B), and also conspicuous depletions (<0.5x: Na, Ca, Zn, Sr, Pb). Data for the Henbury target subgreywacke show that most enrichments and depletions relative to UCC in Henbury glass are characteristics inherited from the target rock, with the notable exceptions of Fe, Ni, and Co, which all have values in the target subgreywacke that overlap with UCC (Fig. 5).

Twenty-eight spot analyses were made in LA-ICP-MS session 2 for siderophile elements (S, Cr, Co, Ni), including three PGE (Rh, Ir, Pt) over the same four areas of the Henbury glass sample (Table 3). Three elements analyzed in session 2 (Cr, Fe, Co, Ni, Cu) were previously analyzed in session 1; mean values for each element in both sessions overlap within 2SD uncertainties, which range from 20 to 50 % (Table 3). The PGE values for Ir range from 0.227 to 3.97 µg/g (avg = 1.45 ± 1.70 µg/g, 2SD), Rh from 0.0372 to 0.224 µg/g (avg = 0.113 ± 0.09 µg/g, 2SD), and Pt from 0.196 to 1.77 µg/g (avg = 0.712 ± 0.71 µg/g, 2σ, based on [194]Pt). Variations about the mean (2SD) for PGE range from 76 to 117 % (Table 3).

Twenty spot analyses were made in LA-ICP-MS session 3 for six PGE (Ru, Rh, Pd, Os, Ir, Pt), all within area 1 of the Henbury sample (Table 4). The PGE abundances ranged from 0.01 to 0.44 µg/g, including (in decreasing order, at 2SD): 0.813 ± 1.74 µg/g (Pt), 0.444 ± 0.86 µg/g (Ir), 0.304 ± 0.59 µg/g (Ru), 0.0888 ± 0.07 µg/g (Pd), 0.0385 ± 0.03 µg/g (Rh), and 0.0108 ± 0.03 µg/g (Os). Variations about the mean (2SD) for PGE range from 74 to 307 % (Table 4).

3.3. Detection of projectile components

3.3.1. Henbury Fe-Si mixing model

A two-component mixing model was constructed for Fe and Si abundances to evaluate mixing between the Henbury target subgreywacke and the projectile (Fig. 6A,B). Average values of 91.95 wt% Fe and 0.1 wt% Si were used for the Henbury iron (Taylor and Kolbe, 1965), and average values of 3.07 wt% Fe and 36.47 wt% Si were used for the target subgreywacke (Taylor, 1967). Glass data include those from this study (n = 32, EMPA) and published values (n = 3, Spencer, 1933; Taylor and Kolbe, 1965). Henbury glass data plot as an array along the mixing line that indicates a significant projectile component (Fig. 6A). Close inspection (Fig. 6B) reveals that most glass data plot parallel to, but slightly offset from, the mixing model towards slightly lower Si values; similar offsets in Fe-Si mixing models noted in prior studies of impact glasses were attributed to indicate the presence of a missing lower-Si target component (Fazio et al., 2016). Other target rock contributions, variations in oxidation state of Fe, undetected molecular components (H_2O, CO_2), and/or low EMPA glass totals (avg = 96.2 wt %) all can influence how well measured values agree with the model. The Fe-Si mixing model indicates that Henbury glass is heterogeneous, and contains regions where the projectile component ranges from 5 to 18 % (avg = 13 %) (Fig. 6B).

3.3.2. Henbury Ni-Co mixing model

A two-component mixing model was constructed for Ni and Co abundances (Fig. 6C,D). Average values of 74,300 µg/g Ni and 4400 µg/ g Co were used for the Henbury iron (Wasson, 1967; Lewis and Moore, 1971), and average values of 21 µg/g Ni and 10 µg/g Co were used for the target subgreywacke (Taylor and McLennan, 1979). Data for Henbury glass include analyses made in this study (n = 25, LA-ICP-MS session 1), two analyses from Taylor and Kolbe (1965), and four additional analyses (Taylor and McLennan, 1979; Attrep et al., 1991). All glass data show systematic covariations of Ni and Co, and plot as a mostly linear array (Fig. 6C). A regression through all Henbury glass

Table 5
EMPA data for Kamil glass spherules (in wt%).

Sample	Si	Fe	Al	Ni	Co
DL	0.04	0.05	0.04	0.05	0.05
S24-KC4-45	26.42	18.69	6.76	1.82	0.09
S24-KC4-45	26.31	18.71	6.62	1.68	0.09
S24-KC4-45	26.29	18.57	6.65	1.81	0.07
S24-KC4-45	26.27	18.85	6.54	2.16	0.07
S24-KC4-45	26.24	18.47	6.95	1.67	0.11
S24-KC4-45	25.77	19.49	6.76	1.91	0.11
S24-KC4-45	24.69	19.49	7.20	1.77	0.08
S24-KC4-45	23.88	21.61	7.35	1.68	bdl
S24-KC4-45	22.96	21.88	7.40	2.25	0.10
S24-KC4-46	22.88	24.24	5.72	3.80	0.13
S24-KC4-46	22.87	26.61	6.41	1.86	0.08
S24-KC4-46	21.79	25.00	6.71	2.94	bdl
S24-KC4-46	21.73	25.95	6.84	2.27	0.16
S24-KC4-46	21.25	27.80	6.58	2.33	0.14
S24-KC4-46	20.98	28.11	4.98	4.67	0.17
S24-KC4-46	20.80	27.68	5.14	4.32	0.12
S24-KC4-46	20.73	28.03	5.31	4.27	0.19
S24-KC4-48	27.94	20.04	7.31	0.89	0.07
S24-KC4-48	20.58	25.04	7.11	2.00	0.06
S24-KC4-48	20.42	25.38	9.11	1.04	bdl
S24-KC4-48	19.47	28.05	7.48	1.87	bdl
S24-KC4-54	25.69	18.16	7.03	2.04	0.07
S24-KC4-54	25.67	17.93	6.99	2.93	bdl
S24-KC4-54	25.61	18.68	7.01	1.96	bdl
S24-KC4-54	25.60	19.14	6.88	1.99	0.10
S24-KC4-54	25.57	18.90	6.85	1.96	bdl
S24-KC4-54	25.49	18.57	7.75	2.09	bdl
S24-KC4-54	25.41	19.18	6.92	2.07	0.10
S24-KC4-54	25.26	19.30	7.28	1.96	0.10
S24-KC4-54	25.21	19.25	7.10	1.73	0.09
S24-KC4-54	24.54	18.44	6.54	2.59	0.09
S24-KC4-56	29.32	18.17	5.95	1.47	0.07
S24-KC4-56	24.34	22.33	6.30	2.74	0.10
S24-KC4-56	23.43	22.12	7.40	2.04	0.09
S24-KC4-56	23.25	22.99	6.55	2.03	0.09
S24-KC4-56	23.19	22.12	7.17	2.47	bdl
S24-KC4-56	23.16	22.86	6.53	2.16	bdl
S24-KC4-56	22.98	23.44	6.87	2.05	bdl
S24-KC4-56	22.82	22.93	7.05	2.15	0.10
S24-KC4-56	22.77	23.46	7.17	1.98	bdl
S24-KC4-56	22.56	22.95	7.06	2.38	bdl
S24-KC4-56	22.24	24.00	7.38	1.57	bdl
S24-KC4-56	22.09	24.25	7.49	1.91	0.12
S24-KC4-56	21.97	23.77	7.30	2.14	0.10
S24-KC4-56	21.96	24.30	7.58	1.75	bdl
S24-KC4-56	21.44	23.62	7.33	2.59	0.11
S24-KC3-91	29.56	17.28	4.12	1.75	bdl
S24-KC3-91	25.55	24.03	5.46	0.52	bdl
S24-KC3-91	25.27	22.99	5.43	0.59	0.07
S24-KC3-91	25.21	22.80	5.28	0.59	bdl
S24-KC3-91	24.87	25.17	5.60	bdl	bdl
S24-KC3-91	24.74	24.60	5.45	bdl	0.07
S24-KC3-91	24.56	25.24	5.53	bdl	bdl
S24-KC3-91	24.44	24.19	5.42	0.94	0.07
S24-KC3-91	24.35	25.09	5.48	0.75	bdl
S24-KC3-91	24.18	25.54	5.42	0.59	0.09
S24-KC3-91	24.17	25.01	5.25	2.06	0.10
S24-KC3-91	23.05	27.13	5.55	1.37	0.06
S24-KC3-91	22.86	26.99	5.45	1.33	bdl
S24-KC3-91	22.61	26.68	5.99	4.22	0.11
S24-KC3-91	22.60	27.69	5.06	1.10	bdl
S24-KC3-91	22.60	25.99	5.27	2.78	0.12
S24-KC3-91	22.32	27.27	5.12	3.49	0.17
S24-KC3-91	22.17	26.61	4.90	4.25	0.16
S24-KC3-91	21.92	26.82	5.09	3.56	0.19
S24-KC3-91	21.80	27.51	5.25	2.68	0.11
S24-KC3-91	21.72	27.73	5.20	3.39	0.18
S24-KC3-91	21.42	30.44	4.98	1.71	0.07
S24-KC3-91	21.18	28.26	4.97	3.23	0.27
S24-KC3-91	20.93	29.71	4.79	1.49	0.09
S24-KC3-91	20.81	25.86	4.27	3.95	0.18

DL = detection limit. bdl = below DL. Spot size = 5 μm.

Table 6
LA-ICP-MS data for Kamil glass spherules (in μg/g).

	Ni	Co
DL	0.17	0.04
S24-KC4-45	16,244	655
S24-KC4-46	13,102	587
S24-KC4-47	27,684	1178
S24-KC4-48	15,440	652
S24-KC5-16	13,668	704
S24-KC5-13	13,377	1410
S24-KC5-9	40,418	1567
S24-KC5-7	16,826	717
S24-KC5-6	29,118	1321
S24-KC5-5	35,414	1509
S24-KC5-3	39,483	1514
S24-KC5-2	19,788	1271
S24-KC5-1	14,875	1028

DL = detection limit. Spot size = 50 μm.

data (n = 31) shows they are highly correlated (R^2 = 0.97); the regression overlaps with and is largely coincident with the mixing model (Fig. 6C). A zoomed in view of Henbury glass data with a projectile component above 3 % abundance, which includes only dark colored glass (Fig. 6D) again reveals a highly correlated data set (R^2 = 0.92, n = 27), which corresponds to a 4 to 15 % projectile component (avg = 10 %).

3.3.3. Henbury Cr-Ir mixing model

Two component mixing models were constructed for Cr and Ir abundances (Fig. 7). One model illustrates mixing of target sub-greywacke and Henbury iron, and the other illustrates mixing of target subgreywacke and chondritic meteorites. Average values of 125 μg/g Cr and 13 μg/g Ir were used for the Henbury iron (Smales et al., 1967; Buchwald, 1975; Wasson et al., 1998; Petaev and Jacobson, 2004; Holdship et al., 2018). Average values of 55 μg/g Cr were used for the target subgreywacke (Taylor and McLennan, 1979); no Ir data are available for the subgreywacke, so a value of 0.02 ng/g Ir for upper continental crust (UCC) was used instead (Taylor and McLennan, 1995). A field for chondritic meteorites was defined extending around average values of 3000 μg/g Cr and 500 ng/g Ir (Wasson and Kallemeyn, 1988), as well as fields for primitive iron meteorites and achondrites (after Tagle and Hecht, 2006). A field encompassing Cr and Ir values for 600 magmatic iron meteorites was defined using data from the MetBase.org meteorite database (Hezel, 2020). Values for mid-ocean ridge basalt (MORB) (Cr = 226 μg/g, Ir = 0.02 ng/g, Rehkämper et al., 1999) and UCC (Cr = 35 μg/g, Ir = 0.02 ng/g, Taylor and McLennan, 1995) are also shown.

Henbury glass data from this study (n = 28, LA-ICP-MS session 2) yields average values of Cr = 75.9 ± 25.6 μg/g (2SD), and Ir = 1.45 ± 1.70 μg/g (2SD) (Table 3). The glass data fall on, or near to, the subgreywacke-iron mixing line and lie entirely inside the field of magmatic iron meteorites (Fig. 7). The absence of any Henbury glass data near the subgreywacke-chondrite mixing line excludes chondrites as a possible projectile, as expected. Henbury glass is heterogeneous in Cr and Ir abundance; modelled projectile contributions range from 2 to 31 %, with an average of 11.5 %. Additional Ir data for the Henbury glass sample from LA-ICP-MS session 3 are also plotted in Fig. 7 (n = 20); given that no correlative Cr data were collected in session 3, the Ir average (0.444 ± 0.86 μg/g, 2SD) and range are plotted as a point anchored to the average Cr value measured in session 2. The two determinations for Ir abundance (1.45 ± 1.70 μg/g vs. 0.444 ± 0.86 μg/g, 2SD) are indistinguishable within uncertainty, and confirm an anomalously high, and heterogeneous, Ir content relative to crustal rocks.

3.3.4. Henbury glass PGE abundance

The Henbury glass LA-ICP-MS session 3 analyses yielded data for six PGE (Table 4), which have been normalized to their values in the
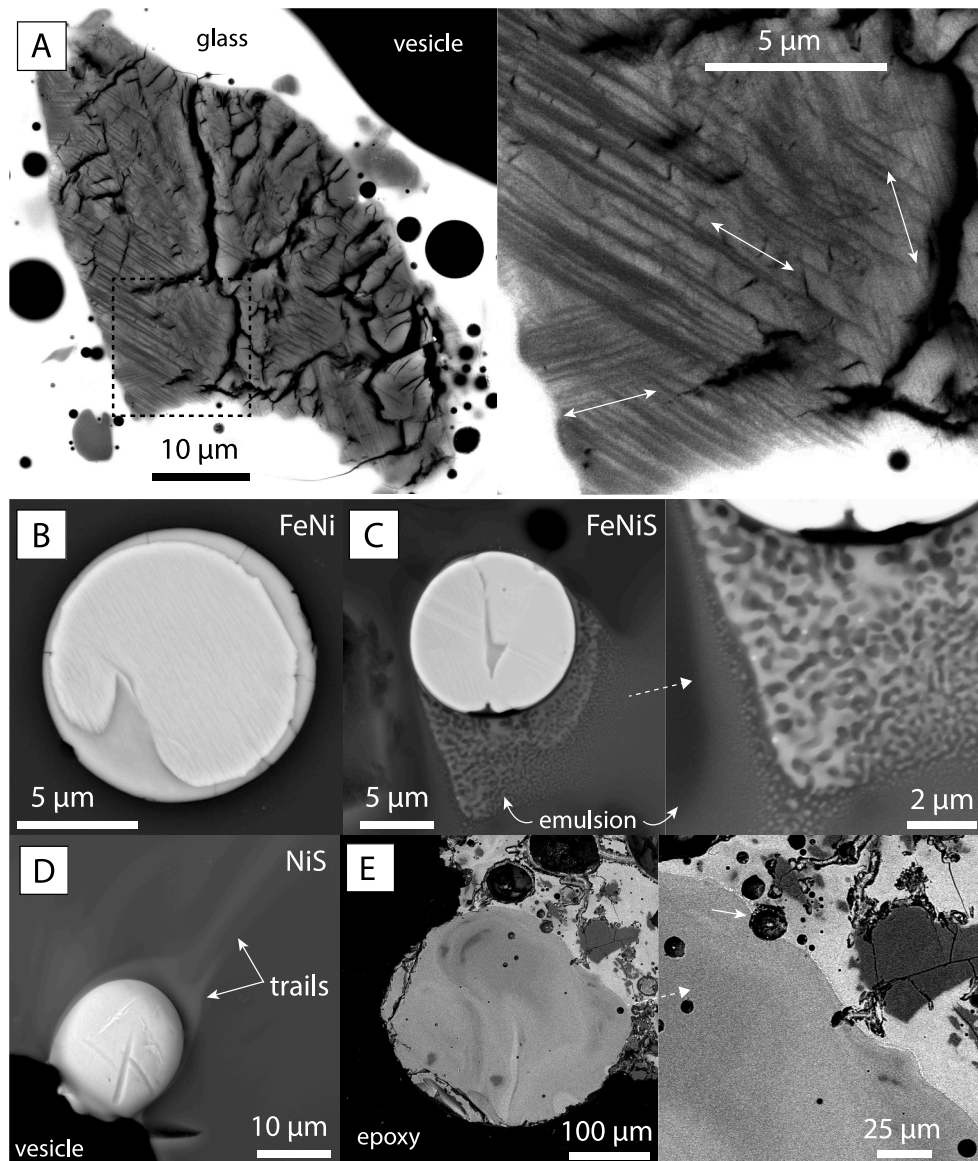
Fig. 2. Backscattered electron images of inclusions in Henbury glass. (A) High contrast image of a fractured quartz grain with at least three orientations of planar deformation features (PDF). (B) Close up view of grain shown in A; arrows indicate orientations of PDF sets. (B-D) Droplets of metal alloys in Henbury glass, including FeNi, FeNiS, and NiS (panel C displays an emulsion texture). (E) Glass spherule accreted to the exterior surface of Henbury impactite. The close-up view shows the spherule surface is locally concave and the contact contains vesicles.

Henbury iron (Fig. 8). Average values used for the Henbury iron include 13.71 ± 3.74 µg/g Ru (n = 3), 2.06 ± 0.547 µg/g Rh (n = 2), 2.31 ± 0.13 µg/g Pd (n = 2), 16.28 ± 0.91 µg/g Os (n = 2), 15.24 ± 4.13 µg/g Ir (n = 2), and 17.67 ± 2.73 µg/g Pt (n = 3) (Wasson, 1967; Holdship et al., 2018; Attrep et al., 1991; Pernicka and Wasson, 1987; Petaev and Jacobsen, 2004; Wasson et al., 1998). Fig. 8 illustrates that the average abundance of projectile-derived PGE in Henbury glass ranges from 0.07 % (Os) to 4.7 % (Pt), with an average of 3.1 % for all PGE, excluding Os; all PGE (except Os) show significant overlap in projectile-normalized abundances (Fig. 8). Ratios of PGE in Henbury glass all appear fractionated from one another relative to their abundance in the Henbury iron, based on evaluation of PGE ratio vs. PGE abundance plots for all measured PGE (Fig. S1). Specific carrier phases for PGE in the Henbury glass sample analyzed were not resolved by imaging in this study; the LA-ICP-MS analyses targeted glassy areas, and avoided minerals exposed on the polished surface.

3.3.5. Kamil and Wabar glasses

To facilitate a comparison of Henbury glass with other glasses from small craters (<1 km) formed by iron meteorites in siliceous target rocks, mixing models for Fe-Si and Ni-Co were constructed for glass from both Kamil and Wabar craters. For Kamil, average values for the projectile (Gebel Kamil ungrouped ataxite) are from Gebelli et al. (2015), values for target rocks are from Folco et al. (2015), and glass data are from Folco et al. (2015), Fazio et al. (2016), and the new EMPA (n = 46) and LA-ICP-MS (n = 17) data reported here (Tables 5, 6). For Wabar crater, values for the projectile (Wabar IIIAB iron) are from Mittlefehldt et al. (1992), values for target rocks are from Hörz et al. (1989), and glass data are from Spencer (1933), Hörz et al. (1989), Mittlefehldt et al. (1992), and Hamann et al. (2013).

Kamil glass shows systematic covariations of Fe and Si and plots as an array along the mixing line, indicating a significant projectile component (Fig. 9A). Most glass data are offset from the mixing model towards slightly lower Si values, similar to Henbury glass; this offset was previously attributed to a kaolinite-rich matrix component (Fazio et al.,
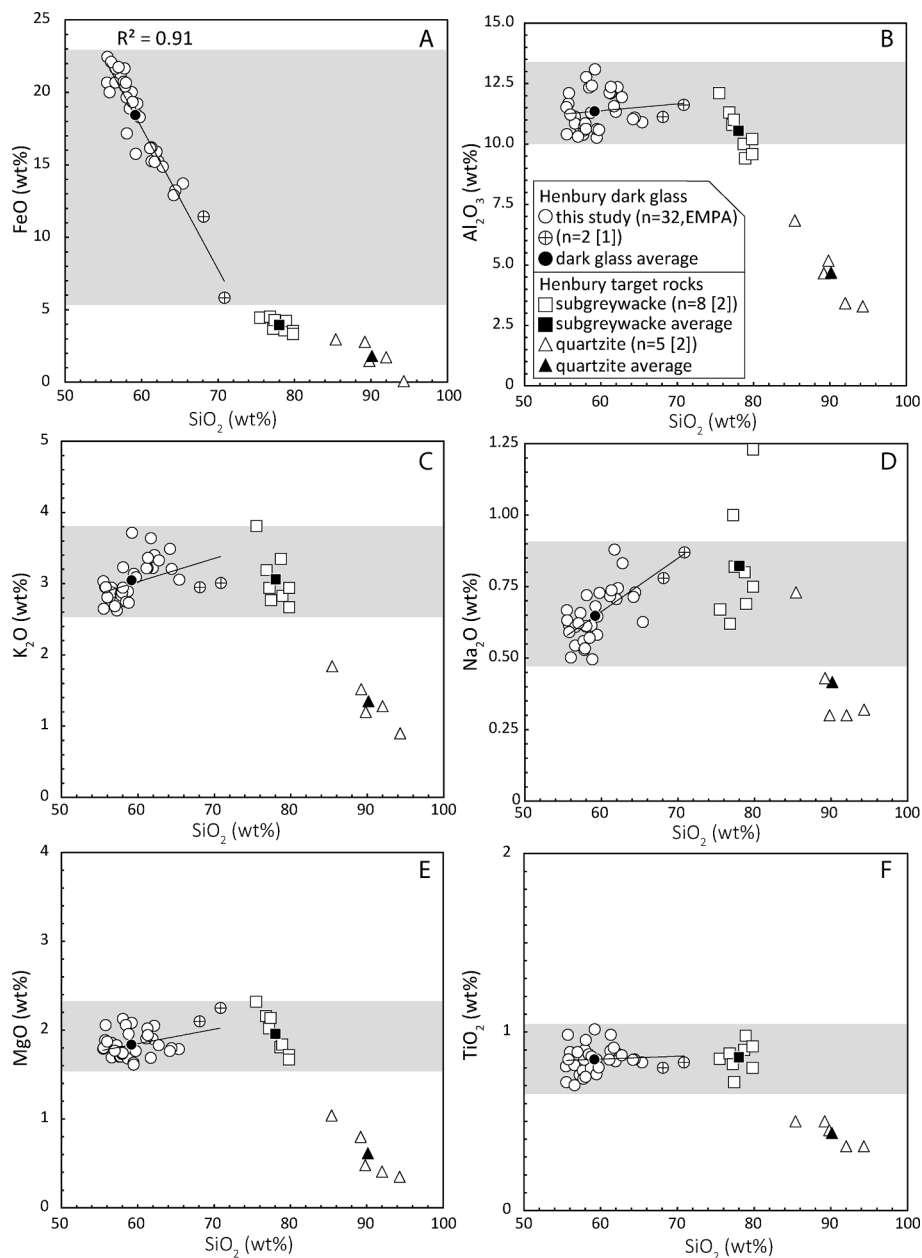
Fig. 3. Harker diagrams for Henbury glass and target rocks. Shaded areas encompass values of Henbury glass. (A) FeO. (B) Al_2O_3. (C) K_2O. (D) Na_2O. (E) MgO. (F) TiO_2. Other data sources: [1] Taylor and Kolbe (1965); [2] Taylor and McLennan (1979).

2016). The Fe-Si values in Kamil glass correspond to a 9 to 37 % projectile component (avg = 28 %) (Fig. 9A). For Ni-Co, Kamil glasses show a large variation of values with significant scatter (Fig. 9B). A regression through all Kamil glass data (n = 60) shows they are poorly correlated (R^2 = 0.52); the regression is subparallel to the mixing line at a meteoritic abundance > 5 % and diverges from the mixing line at lower values (Fig. 9B). The Kamil glass Ni-Co values correspond to a 3 to 23 % projectile component (avg = 11.5 %).

Wabar glass also shows systematic covariations of Fe and Si; in contrast to Henbury and Kamil glass, all Wabar glass data plot directly along the mixing line (Fig. 9C). The Fe-Si values in Wabar glass correspond to a 1.5 to 13 % projectile component (avg = 8 %) (Fig. 9C). For Ni-Co, Wabar glass data are scattered and poorly correlated (R^2 = 0.29, n = 26); the regression is subparallel to but offset from the mixing line (Fig. 9D). Wabar glass Ni-Co values correspond to a 4 to 9 % projectile component (avg = 6.5 %).

4. Discussion

4.1. New insights on Henbury impact glass

Early geochemical studies of Henbury glass were largely driven by Ross Taylor and colleagues, with a focus on comparison with other impact glasses, and also on identifying the target rock component. The high iron content was recognized as meteoritic, and corrections were applied to remove the projectile component (Taylor and Kolbe, 1965; Taylor, 1966, 1967). Compositional data reported here are generally in agreement with published data and show the Henbury impactite is an intermediate composition iron-rich silicate glass that ranges from ferroan andesite to dacite (Figs. 3-4). Harker diagrams show that Henbury glass has a strong geochemical affinity to the subgreywacke target rocks and bears little resemblance to quartzite target rocks (Taylor, 1967; Taylor and McLennan, 1979); iron is the only major element that cannot be wholly attributed to originating from the target rocks (Fig. 3).
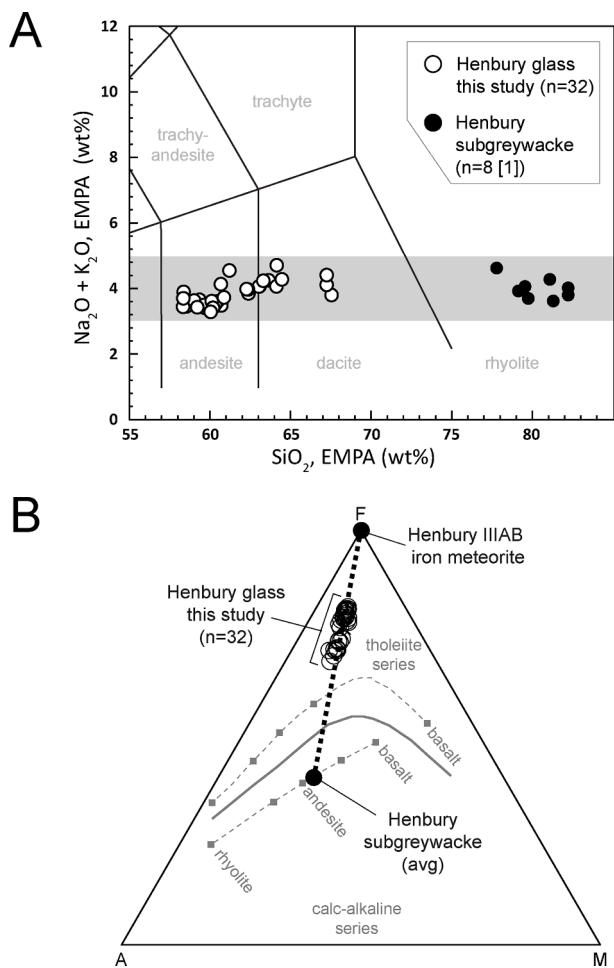
Fig. 4. Igneous classification diagrams for Henbury glass. A. Total alkali vs silica (TAS) diagram (LeBas et al., 1986). B. Alkali-iron-magnesium (AFM) diagram (Irvine and Baragar, 1971). Other data sources: [1] Taylor and McLennan (1979).

The predominance of subgreywacke exposed in the walls of crater 7a, in contrast to crater 7b which exposes quartzite, suggests the glass analyzed here was most likely ejected from crater 7a (Fig. 1A), a conclusion made previously in studies of other Henbury glasses (Taylor, 1967). The deformed glass spherule accreted to the exterior surface of the larger impactite (Fig. 2E) indicates a dynamic collision of two molten objects.

Crystalline materials in Henbury impactite have received less attention than glass. Ding and Veblen (2004) used transmission electron microscopy to describe dendritic fayalite, magnetite, and hercynite as newly formed quenched crystals in Henbury glass. The same authors also reported abundant euhedral diamond, up to a few hundred nm in size, which were interpreted to have formed by vapor phase deposition, rather than shock compression (Ding and Veblen, 2004). The presence of α-quartz was also noted. All crystalline phases reported by Ding and Veblen (2004) were sub-micrometer in size; in contrast, quartz grains up to 50 μm in size are abundant in the sample analyzed in this study. The discovery of shock microstructures in quartz (Fig. 2A) represents the first description of a shock-metamorphosed mineral from the Henbury crater field; ongoing studies to determine PDF orientations will be reported elsewhere.

4.2. Detection of projectile components from iron meteorites

The dark iron-rich silicate glasses described here are characteristic glasses produced when iron meteorites form small (<1 km) impact craters in siliceous targets rocks. Such glass is ideal for detection of projectile contamination, given the large contrast in composition of the fused materials (e.g., Mittlefehldt et al., 1992; Ebert et al., 2013; 2014; Fazio et al., 2016; Hamann et al., 2018). The low abundance of siderophile elements in most siliceous supracrustal rocks, along with the low abundance of silica in most iron meteorites, allows unambiguous detection of projectile components through elemental abundances and ratios (Figs. 3–10).

Previous studies of dark colored impact glasses have shown that projectile-derived elemental abundances based on Fe, Ni, and Co in glass from Kamil crater range from 11 to 12 % (Fazio et al., 2016), and at Wabar crater projectile abundances range from 4 to 11 % (Mittlefehldt et al., 1992). Analysis of Kamil and Wabar glass data for Fe-Si and Ni-Co
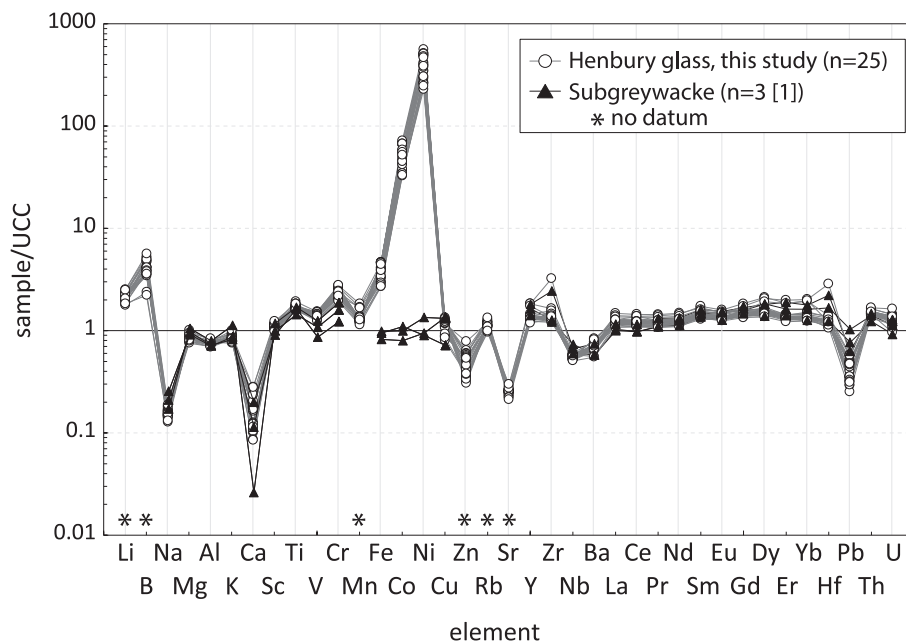
Fig. 5. Major, minor, and trace element data for Henbury glass (this study, LA-ICP-MS session 1) normalized to the upper continental crust (UCC). Also plotted are data for the Henbury subgreywacke target rocks. Other data sources: [1] Taylor and McLennan (1979). UCC values from Taylor and McLennan (1995).
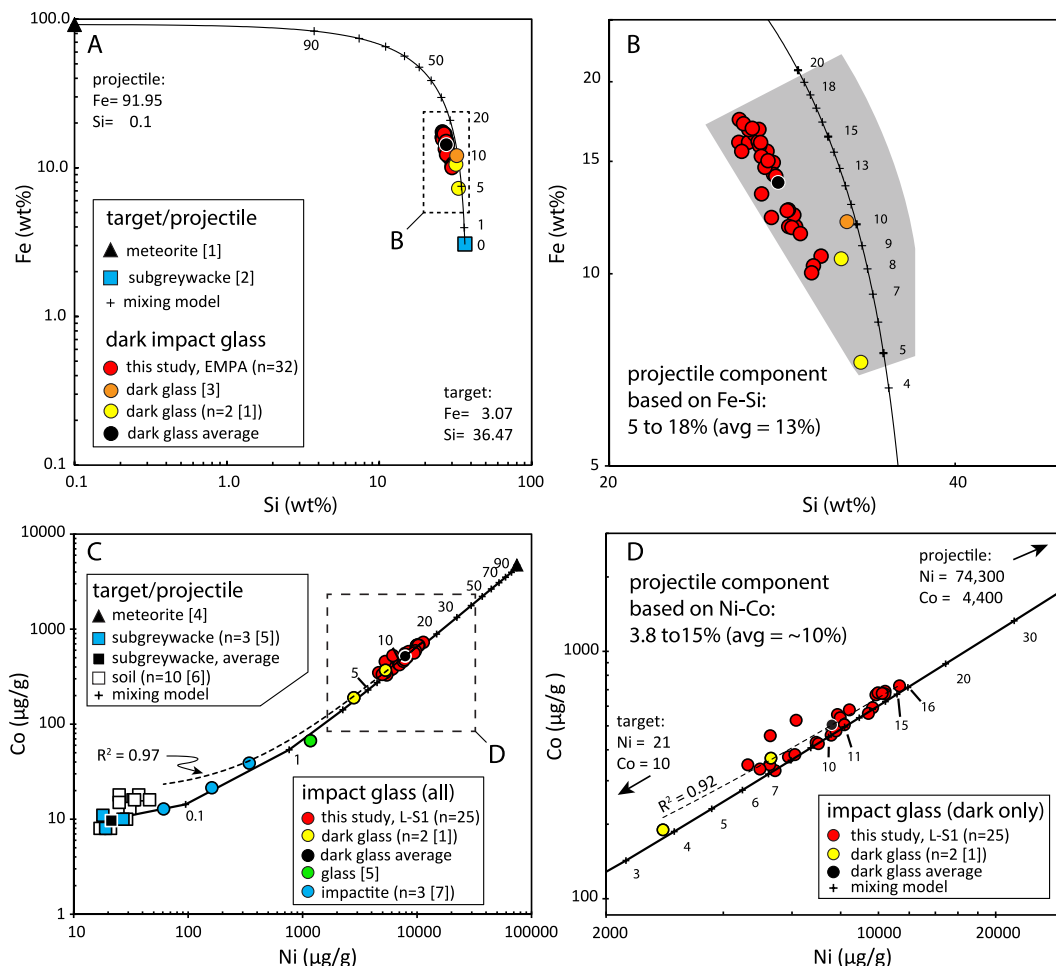
Fig. 6. Covariation diagrams for Henbury glass. (A, B) Electron microprobe analyzer (EMPA, this study) data for Fe and Si plotted on a two-component mixing model for the Henbury subgreywacke target rocks and Henbury IIIAB iron meteorite projectile. (C, D) Laser ablation- inductively coupled plasma-mass spectrometry (LA-ICP-MS) data for Co and Ni plotted on a two-component mixing model for the Henbury subgreywacke target rocks and Henbury IIIAB iron meteorite projectile. Other data sources: [1] Taylor and Kolbe (1965); [2] Taylor (1967); [3] Spencer (1933); [4] Wasson (1967, Lewis and Moore (1971); Wasson et al., 1998 [5] Taylor and McLennan (1979); [6] Hopper et al. (1990); [7] Attrep et al. (1991). L-S1 = LA-ICP-MS session 1 (this study).
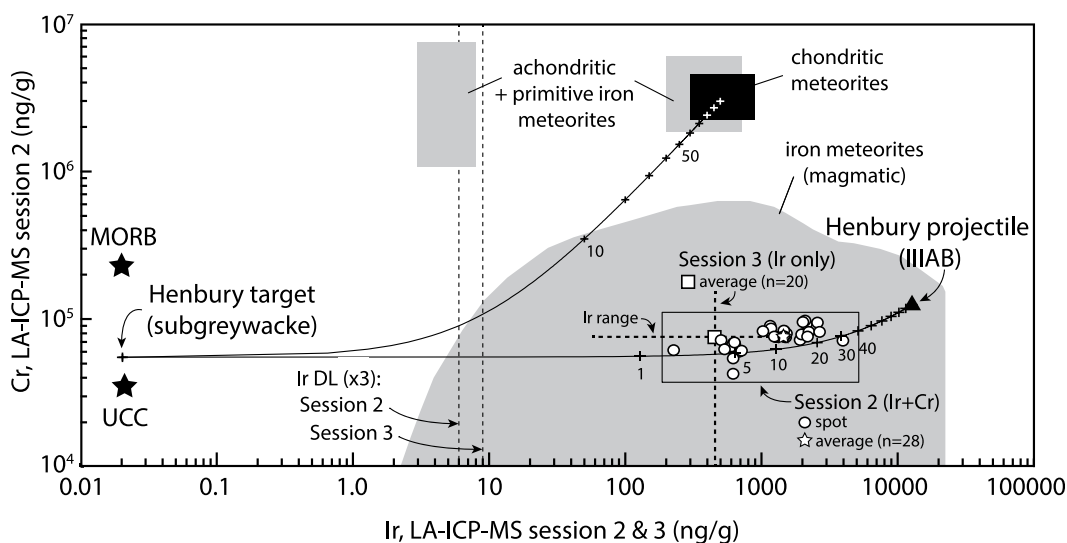
Fig. 7. Covariation diagrams for Cr and Ir in Henbury glass. Laser ablation-inductively coupled plasma-mass spectrometry (LA-ICP-MS) data from this study (LA-ICP-MS sessions 2 & 3). Mixing models for the Henbury subgreywacke target rocks, and chondritic meteorites and the Henbury IIIAB iron are also shown (see text for references). The data in the rectangle show the spread of Henbury glass data (LA-ICP-MS session 2) along the mixing model. The dashed line shows the spread of Ir data from LA-ICP-MS session 3, anchored to the average Cr value from session 2. MORB = mid-ocean ridge basalt; UCC = upper continental crust.
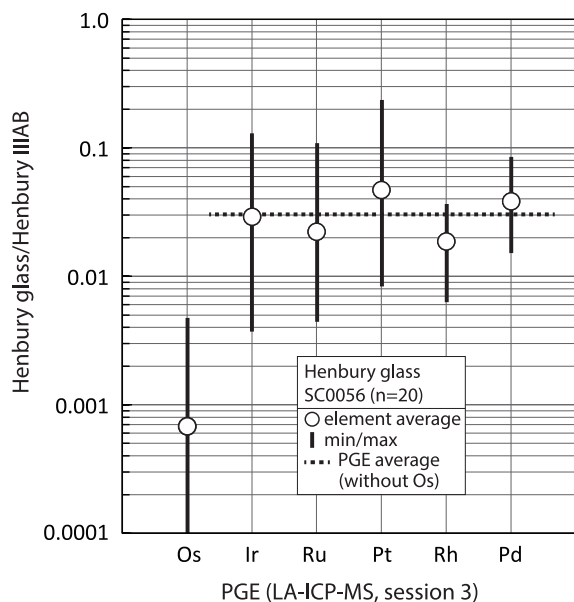
Fig. 8. Average abundance of platinum group elements (PGE) in Henbury glass measured in this study (LA-ICP-MS session 3), normalized to the Henbury IIIAB iron (see text for references). Heavy vertical bars indicate range measured for each element. The dashed horizontal line at 0.03 (3.1%) indicates the average projectile PGE abundance in the Henbury glass sample.

presented here (Fig. 9) confirms high projectile abundances are present, with averages for Kamil glass of 28 % (Fe-Si) and 11.5 % (Ni-Co) (Fig. 9A, B), and averages for Wabar glass of 8 % (Fe-Si) and 6.5 % (Ni-Co) (Fig. 9C, D). Data for Henbury glass (Figs. 6–8) also yields high average projectile abundances, including 13 % (Fe-Si), 10 % (Ni-Co), 11.5 % (Cr-Ir), and 3 % (PGE). The total range of estimated projectile component for each of the four proxies evaluated here show considerable variation, reflecting the highly heterogenous composition of the glass. The four independent estimates for Henbury glass collectively suggest an average projectile abundance of ~ 10 %, with local domains containing higher or lower abundances. Glasses from Kamil, Wabar, and Henbury thus all have substantially higher projectile abundances as compared to impact melt rocks reported from larger impact structures (>1 km), that with a few notable exceptions, are typically < 1 % (Koeberl, 2014; Goderis et al., 2013). Impact glasses with such high projectile abundances must also have formed at larger impact craters, however they likely represent a much smaller fraction of total melt produced, relative to that produced at the small craters discussed here.

4.3. Fractionation of projectile components in impact melts

Prior studies have described textural observations, such as metal spherules and emulsion textures, and also geochemical evidence, such as non-meteoritic siderophile element ratios, as evidence that projectile components in impact melts rapidly become fractionated prior to quenching. A comparison of these features for glasses from the Henbury, Kamil, and Wabar craters is presented below.

4.3.1. Significance of Ni-rich metal spherules

Metal spherules have been reported in impact glasses from the Henbury, Kamil, and Wabar craters, as well as other localities (e.g., Brett, 1967; El Goresy, 1968; Gibbons et al., 1976). Metal spherules are rare in the Henbury glass analyzed in this study (Fig. 2B-D); the few observed represent fractionated meteoritic residues, as their elemental compositions (determined qualitatively by energy dispersive spectroscopy) are dominated by Fe-Ni, Fe-Ni-S, and Ni-S. The qualitative determinations are consistent with published data that show Henbury metal spherules are rich in Fe (9–77 %) and especially Ni (20–94 %) (El

Goresy, 1968; Gibbons et al., 1976). Metal spherules from Kamil crater (Fe = 41–75 %; Ni up to 94 %) (Folco et al., 2015, 2022) and Wabar crater (Fe = 37–82 %; Ni up to 60 %) (Hamann et al., 2013) are also highly enriched in meteoritic Ni. The size of metal spherules in glasses from the three sites varies considerably; the largest metal spherules in Henbury glass observed in this study are ~ 10 μm, whereas metal spherules in Wabar glass are up to 100 μm (El Goresy, 1968; Hamann et al., 2013), and they are up to 200 μm in Kamil glass (Fazio et al., 2016).

Various processes have been proposed to form metal spherules, including atmospheric projectile melting, selective shock melting, condensation from metal vapor, projectile decompression, and selective Fe oxidation (see Kelly et al., 1974; Gibbons et al., 1976; Mittlefehldt et al., 1992). The Ni enrichment of metal spherules in impact glass can be extreme (>90 %), far beyond meteoritic abundances (El Goresy, 1968; Gibbons et al., 1976). Many studies have concluded that meteoritic Fe is preferentially fractionated by selective oxidation to FeO$_x$, which then dissolves into glass and leaves Ni-rich (±Co, S, P) meteoritic metal spherules behind (e.g., Brett, 1967; Kelly et al., 1974; Gibbons et al., 1976; Ebert et al., 2014; Fazio et al., 2016). At what stage during the overall impact process the projectile fractionates due to oxidation remains a matter of debate. Some studies cite the lack of Fe-enrichment in glass adjacent to metal spherules, metal spherules in soil samples, and unfractionated target rock components to argue that fractionation of projectile-derived Fe takes place in the atmosphere prior to mixing of meteoritic material into glass (Gibbons et al., 1976; Mittlefehldt et al., 1992; Badyukov and Raitala, 2012). At crater fields such as Henbury, where at least 13 craters have been identified, atmospheric break-up may have provided the opportunity for enhanced oxidation of meteoritic Fe. Other studies cite extensive Fe-rich emulsion textures as evidence for oxidation and fractionation of projectile material in-situ within the glassy impactite (Hamann et al., 2013). Given the compelling textural evidence for both ex situ (atmospheric) and in situ (within glass) fractionation of meteoritic Fe, it seems likely that both processes can occur.

A recent study of metallic spherules in soil from Kamil crater proposes that the metal spherules initially form within impact glass as immiscible projectile residues due to selective oxidation of Fe, which partitions into the melt; in this case, the resulting Ni-rich spherules are interpreted as immiscible projectile-derived droplets (Folco et al., 2022). Folco et al. (2022) presented textural evidence to bolster the argument for in situ (within glass) formation of the metal spherules, including documenting glass rims on spherules in soil, and showing 'frozen in' metal spherules protruding from spherules, to argue that once formed, the Ni-rich spherules can become physically separated from the glass. Physical separation of the metal spherules after Fe oxidation as described by Folco et al. (2022) represents a mechanical fractionation of Ni-rich meteoritic components from impact glass. Similar 'frozen in' Ni-rich metallic spherules have also been documented emerging from a Henbury glass spherule found in a soil sample (Hopper et al., 1990), which suggests that mechanical fractionation and separation of Ni-rich projectile residue may be a common process.

To evaluate if evidence of siderophile element depletion (Ni, Co) related to metal spherule formation/fractionation can be detected in the studied glasses, we constructed two component ratio mixing models for Fe:Ni and Ni:Co using glass data from the Henbury, Kamil, and Wabar craters (Fig. 10). The siderophile element ratio mixing curves for all three sites show that mixing small amounts of projectile (<1%) into target rock melts produces ratios that are dominated by the projectile. For both Kamil and Wabar, mixing 10 % projectile into target rock melts yields ratios that are indistinguishable from the projectile. However, glass samples from the three sites show systematic differences in siderophile element ratio behaviour. The mixing curves show that Henbury glass clusters close to the Henbury iron; the average Fe:Ni (17.6) and Ni:Co (15.1) plot near the projectile, with most data plotting below the mixing line (Fig. 10A). Kamil glass shows more scatter (average Fe:Ni = 15.0; Ni:Co = 19.7), with most data plotting below the mixing line
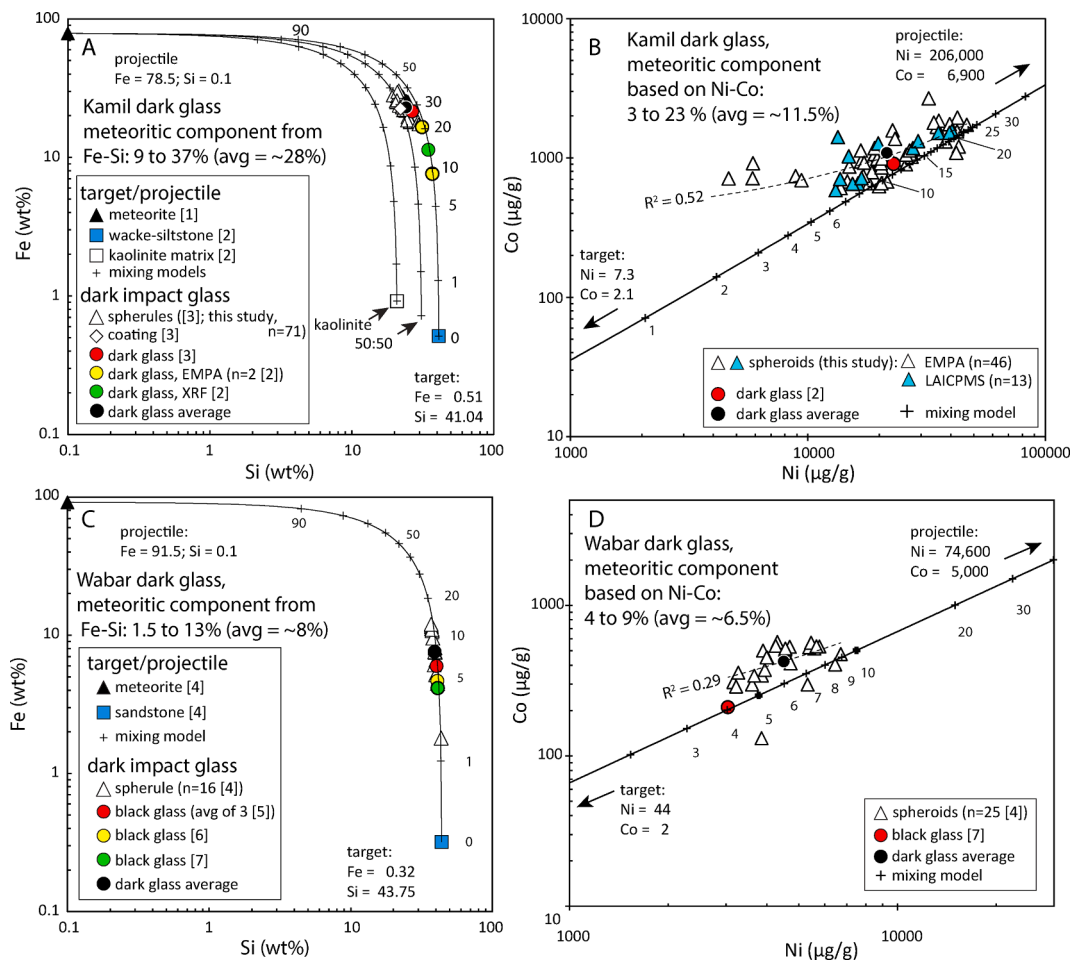
Fig. 9. Covariation diagrams for glass from Kamil and Wabar craters. (A, B) Data for Fe-Si and Ni-Co in Kamil glass plotted on two-component mixing models for target rocks and the Gebel Kamil ataxite projectile. (C, D) Data for Fe-Si and Ni-Co in Wabar glass plotted on two-component mixing models for target rocks and the Wabar IIIAB iron projectile. Other data sources: [1] Gemelli et al. (2015); [2] Fazio et al. (2016); [3] Folco et al. (2015); [4] Mittlefehldt et al. (1992); [5] Hamann et al. (2013); [6] Spencer (1933); [7] Hörz et al. (1989).

(Fig. 10B). Wabar glass shows more scatter than Henbury but less than Kamil (average Fe:Ni = 20.9; Ni:Co = 10.7), with most data plotting below the mixing line (Fig. 10C). Glasses from all three sites thus define conspicuous trends that range from meteoritic values towards higher Fe:Ni and lower Ni:Co ratios. In the case of Henbury and Kamil glass, the trajectories trend broadly towards target rock values (Fig. 10A,B), however the trajectory of Wabar glass trends towards values that are substantially below target rock values (Fig. 10C).

The magnitude of the fractionation of projectile-derived siderophile elements (Fe-Ni-Co) in glasses from the three impact sites was calculated by normalizing the projectile ratios with the estimated projectile-derived contribution in the glass. Target rock contributions of Fe, Ni, and Co in the glass were assumed to be present at $\sim$ 90 % of values indigenous to the target rocks, and were removed from the glass data (Table 7). In general, effectively all Ni and Co in the glass samples is assumed to be meteoritic in origin, given the extremely low values of Ni and Co in the target rocks (2 to 44 μg/g, Figs. 6, 9; Table 7). In contrast, target rock contributions of Fe to the glasses are more variable. For Kamil (0.51 wt% Fe) and Wabar (0.32 wt% Fe), target rock contributions of Fe to glass are minor, in comparison with Henbury target rocks, which contribute 3.07 wt% Fe to glass. Estimated projectile-derived siderophile element ratio fractionation trends for average glass values from each site are shown in Fig. 11. It is readily apparent that both Ni and Co are strongly fractionated from Fe based on Fe:Ni and Fe:Co ratios, which define trends with a negative slope. Henbury glass represents the least fractionated (3.3 % Co to 5.9 % Ni) and Kamil glass the most

fractionated (46 % Co to 64 % Ni) (Fig. 11; Table 7), with Ni consistently more fractionated than Co. The preferential loss of meteoritic Ni relative to Co is also reflected in Ni:Co ratios, which define a trend with a positive slope, recording progressively more meteoritic Ni-loss relative to Co in glass from each of the three sites (Fig. 11).

We propose that the observed Ni and Co depletion trends for glasses for all three sites result from the extent of formation and subsequent physical fractionation of Ni-rich metal spherules from the glass. Among samples considered here, the Henbury glass analyzed in this study represents the least fractionated glass, as it contains few metal spherules, the metal spherules observed are small (up to 10 μm), the glass preserves the most systematic covariation of meteoritic Ni and Co abundance (Fig. 6D), and the glass records the smallest magnitude of inferred Ni (6 %) and Co (3.3 %) loss based on siderophile element ratios (Table 7; Fig. 10A, 11). In contrast, Kamil glass samples represent the most fractionated glasses, as they contain the largest metal spherules (up to 200 μm), show the most scatter in Ni and Co abundances (Fig. 9B), and record the largest magnitude of inferred Ni (64 %) and Co (46 %) loss (Table 7; Fig. 10B, 11). Wabar glass is more fractionated than Henbury glass, yet less fractionated than Kamil glass; it has metal spherules of intermediate size (up to 100 μm), and records an intermediate magnitude of inferred Ni (38 %) and Co (14 %) loss (Table 7; Fig. 9D, 10C, 11).

4.3.2. PGE in Henbury glass

The presence of a significant projectile component ($\sim$10 %) in glasses from Henbury, Kamil, and Wabar craters based on Fe-Si and Ni-
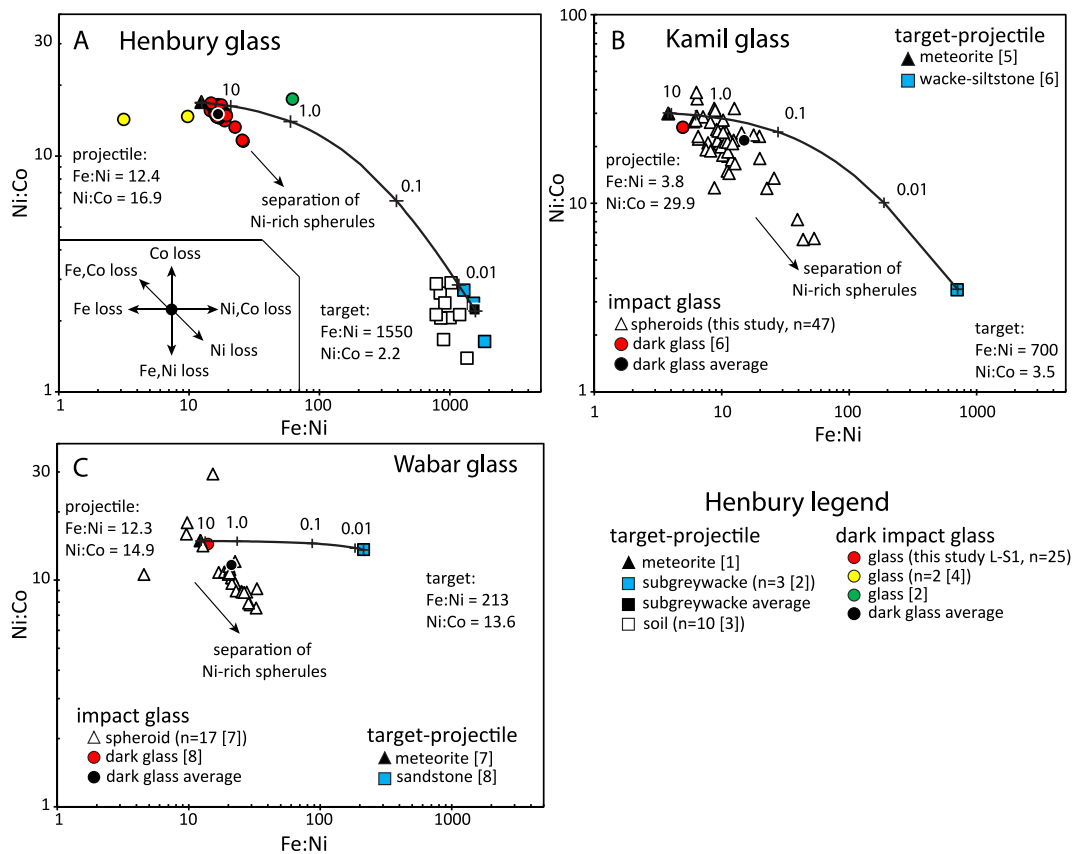
Fig. 10. Covariation diagrams for Ni:Co and Fe:Ni ratios in glass from the Henbury, Kamil, and Wabar impact craters. (A) Henbury glass (this study). (B) Kamil glass (includes new data from this study). C: Wabar glass. Values listed along the mixing curves indicate percent of projectile. Other data sources: [1] Wasson (1967), Lewis and Moore (1971); [2] Taylor and McLennan (1979); [3] Hopper et al. (1991); [4] Taylor and Kolbe (1965); [5] Gemelli et al. (2015); [6] Fazio et al. (2016); [7] Mittlefehldt et al. (1992); [8] Hörz et al. (1989).

Co abundances indicates that these glasses are also likely to have elevated PGE abundances. Abundance data for PGE in Henbury glass reported here range from 1.9 to 4.7 % relative to that in the Henbury IIIAB iron except for Os, which is anomalously depleted relative to the other PGE (Fig. 8). The PGE in Henbury glass are heterogeneous in distribution, and average projectile abundances differ by a factor of ~ 2.5. Few PGE data are available for Wabar or Kamil glass for comparison (cf. Hörz et al., 1989). For a projectile abundance of 5 to 10 %, Wabar glass is predicted to contain from 0.41 to 0.81 µg/g Ir based on 8.15 µg/g Ir reported for the Wabar iron (Mittlefehldt et al., 1992); a single value of 0.308 µg/g Ir in Wabar glass reported by Hörz et al. (1989) is within uncertainty of this range. The PGE data for Henbury glass (this study) and Wabar glass (Mittlefehldt et al., 1992) are variable (Henbury), yet are within a factor of 2–3 of that predicted by Fe-Si and Ni-Co values for the projectile.

4.3.3. Immiscible liquids

Silicate liquid immiscibility has been increasingly recognized as evidence of fractionation processes in impact glasses (Dence et al., 1974; Zolensky and Koeberl, 1991; Pratesi et al., 2002; Hamann et al., 2018). Emulsion textures with Si-rich and Fe-rich silicate glasses have been documented in dark colored impact glass from both Kamil (Fazio et al., 2016) and Wabar (Hamann et al., 2013) craters, and represent either the mingling of initial immiscible liquids, or the unmixing of Fe-rich melt components from Si-rich melt prior to quenching (see discussion in Hamann et al., 2018). In contrast to Wabar and Kamil glasses, occurrences of emulsion textures are rare in the Henbury glass sample analyzed here; they were only observed adjacent to one of the rare metal spherules (Fig. 2C). Emulsion textures characteristically form in glasses with compositional ranges that fall within a miscibility gap ('two liquid

field') at high temperatures (Hamann et al., 2018). Compositional data for Henbury glass reported here were plotted on the quasi-ternary plot of $(CaO-MgO-FeO-TiO_2-P_2O_5)-(Na_2O-K_2O-Al_2O_3)-(SiO_2)$ of Hamann et al. (2018), along with data for Kamil and Wabar glasses (Fig. 12). Henbury glass plots as a cluster in the central two-liquid field, with slightly higher SiO_2 values compared to Kamil bulk glass (Fig. 12), and at lower SiO_2 values compared to Wabar bulk glass; both Henbury and Kamil glasses are higher in the $(Na_2O-K_2O-Al_2O_3)$ component compared to Wabar glass. The absence of widespread emulsion textures in the Henbury glass analyzed here, despite it having a bulk composition within the two-liquid field (Fig. 12), is additional evidence that the Henbury glass analyzed here cooled more rapidly than glasses reported from Kamil and Wabar craters.

4.4. Glassy ejecta at small impact craters- the concept of interface melts

The nature of the target-projectile interface at small impact craters has been described based on glasses produced in impact experiments (Ebert et al., 2014) and glasses from small impact craters (e.g., Hörz et al., 1989; Mittlefehldt et al., 1992; Hamann et al., 2013; Fazio et al., 2016). The target-projectile interface is a complex zone where maximum shock pressures and temperatures are focused during the contact and compression stage of an impact (Melosh, 1989; Ebert et al., 2014). Impact glasses result from a range of dynamic melting, mingling, mixing, oxidation, and unmixing processes between the projectile and target rock(s), producing liquids that are unlikely to achieve chemical homogeneity prior to quenching (Hamann et al., 2018). Melted projectile components are mixed with molten target rock that contains minerals that experienced the highest grade of shock metamorphism (Fig. 13). Projectile-rich melt is then ejected during crater excavation, forming

Table 7
Siderophile elements (in µg/g) and ratios in the studied impact glasses.

Material	Henbury	Wabar	Kamil	Source
Fe data (average values)				
[Fe] in projectile	919,500	915,000	785,000	[1–6,7,8]
[Fe] in glass	131,000	91,950	234,600	[9,7,9]
[Fe] in target	30,700	3200	5100	[10,7,11]
estimated target [Fe] in glass (90 %)	27,630	2880	4590	
estimated projectile [Fe] in glass	103,370	89,070	230,010	
Ni data (average values)				
[Ni] in projectile	74,300	74,600	206,000	[1–6,7,8]
[Ni] in glass	7860	4500	21,500	[9,7,9]
[Ni] in target	21	44	7.3	[12,7,11]
estimated target [Ni] in glass (90 %)	18.9	39.6	6.57	
estimated projectile [Ni] in glass	7841	4460	21,493	
Co data (average values)				
[Co] in projectile	4400	5000	6900	[1–6,7,8]
[Co] in glass	520	420	1090	[9,7,9]
[Co] in target	10	2	2.1	[12,7,11]
estimated target [Co] in glass (90 %)	9	1.8	1.89	
estimated projectile [Co] in glass	511	418	1088	
Estimated Fe:Ni fractionation				
Fe:Ni in projectile	12.4	12.3	3.8	
Fe:Ni in glass	17.6	20.9	15.0	
Fe:Ni projectile-in-glass (estimated)	13.2	20.0	10.7	
Fe:Ni (projectile)/(projectile-in-glass)	0.94	0.62	0.36	
% fractionation (Ni-loss)	**5.9**	**38.4**	**64.5**	
Estimated Fe:Co fractionation				
Fe:Co in projectile	209	183	114	
Fe:Co in glass	252	219	215	
Fe:Co projectile-in-glass (estimated)	202	213	211	
Fe:Co (projectile)/(projectile-in-glass)	1.03	0.86	0.54	
% fractionation (Co-loss)	**3.3**	**14.1**	**46.2**	
Estimated Ni-Co fractionation				
Ni:Co in projectile	16.9	14.9	29.9	
Ni:Co in glass	15.1	10.7	19.7	
Ni:Co projectile-in-glass (estimated)	15.3	10.7	19.8	
Ni:Co (projectile)/(projectile-in-glass)	1.10	1.40	1.51	
% fractionation (Ni-loss)	**10.0**	**39.9**	**51.1**	

Data sources, separated by site: [1] Alderman, 1932; [2] Spencer, 1933; [3] Lewis and Moore, 1971; [4] Buchwald, 1975; [5] Wasson et al., 1998; [6] Taylor and Kolbe, 1965; [7] Mittlefehldt et al., 1992; [8] Gemelli et al., 2015; [9] this study (Tables 2, 4, 5); [10] Taylor, 1967; [11] Fazio et al., 2016; [12] Taylor and McLennan, 1979.

glassy impactite; such glasses are thought to originate from a narrow zone that is likely less than 1 m wide at small craters (e.g., Kamil, Fazio et al., 2016).

Glasses from the Henbury (145 m), Kamil (45 m), and Wabar (110 m) craters are viewed as samples of 'interface melts', as they all have significant projectile contributions and likely originated from similar sized target-projectile interface crater environments. As documented here, glasses from the three sites show significant textural and compositional differences that likely reflect disparate cooling paths in the short time between formation and quenching, although it is also possible that different mixing conditions also occurred, such as atmospheric oxidation of Fe and/or within glass oxidation (Fig. 13A,B, Kelly et al., 1974;
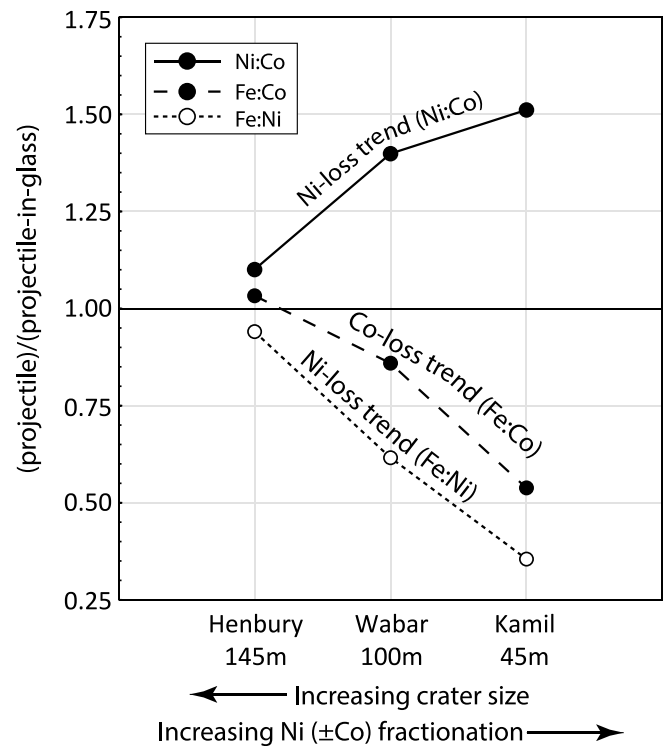
Fig. 11. Estimated fractionation of projectile-derived siderophile element ratios for Fe-Ni-Co in impact glass from the Henbury, Wabar, and Kamil craters.

Gibbons et al., 1976; Mittlefehldt et al., 1992). We propose that Henbury crater glass described here can be considered as a near 'primary' interface melt, in the sense that it represents a relatively more homogenized target-projectile mixture that contains a significant projectile contribution (~10 %) yet experienced little fractionation of the projectile component (Fig. 11). Shocked quartz grains with PDF are preserved in Henbury glass (Fig. 2A), which implies the melt quenched before all shocked quartz grains were fully transformed to lechatelierite. Dark glasses from Wabar and Kamil craters are here considered to represent more 'evolved' interface melts, in the sense that they also contain significant projectile contributions (~10 %) yet record more textural and chemical evidence of projectile fractionation processes (Fig. 13C). Shocked quartz grains have not been reported in dark glass from Wabar, where lechatelierite is common (Hörz et al., 1989; Mittlefehldt et al., 1992; Hamann et al., 2013), whereas at Kamil crater both shocked quartz grains and lechatelierite have been described in black glass (Fazio et al., 2016). In the case of Henbury glass described here, multiple observations indicate that minimal phase separation processes occurred prior to quenching, including the small number and size (<10 µm) of metal spherules, the paucity of both emulsion textures and evidence of liquid immiscibility despite a bulk composition that falls in a miscibility gap at high temperature (Fig. 12), and nearly unfractionated meteoritic Fe:Ni, Fe:Co, and Ni:Co ratios (Figs. 10, 11). In contrast, Kamil and Wabar glasses record more evidence of phase separations prior to quenching, including more and larger (100 to 200 µm) metal spherules, more occurrences of emulsion textures with documented evidence of silicate liquid immiscibility (Hamann et al., 2013; Fazio et al., 2016), and more fractionated Fe:Ni, Fe:Co, and Ni:Co ratios (Figs. 10, 11).

A few caveats of the 'primary' vs 'evolved' interface melt concept for iron-rich silicate impact glasses described above deserve further mention. The first is that the more rapid cooling history inferred for the Henbury glass sample described here may not be representative of all glass produced during the Henbury impact event. Metal spherules have been described in Henbury soil samples (Hodge and Wright, 1971); if they originated in glass and were subsequently separated from glass
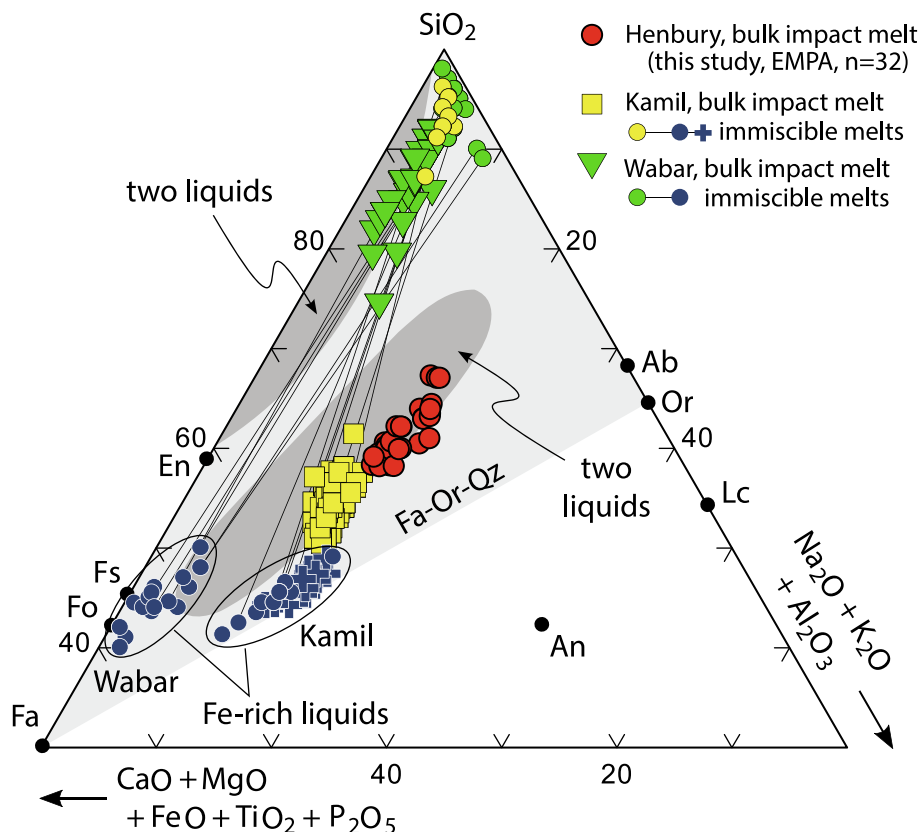
Fig. 12. Pseudoternary diagram showing the composition of impact glass from the Henbury, Kamil, and Wabar craters (after Hamann et al., 2018). Note the similarity in composition of bulk glass for Henbury and Kamil craters.

during ejection via the oxidation-separation process described here (e. g., Folco et al., 2022), it follows that other glass at Henbury must have experienced more significant chemical (and mechanical) fractionation processes than that reported here (cf. El Goresy, 1968). Another caveat is that the observed differences between Henbury glass and the glasses from the other two small craters are here primarily attributed to the faster quenching of Henbury glass, which prevented extensive phase separation processes from occurring. However, all three craters are similar in size (45 to 145 m) and have similar projectile-target characteristics (iron meteorite-sandstone). It is therefore difficult to envision why cooling rates alone of ejected glass would vary significantly among the three sites. One critical aspect of the fractionation process inferred to cause Ni depletion in the various impact glasses is the role of preferential iron oxidation in formation and separation of the Ni-rich metal spherules within glass, and whether it occurs primarily in the atmosphere (Fig. 13A), or within impact glass (Fig. 13B) (Ebert et al., 2014; Folco et al., 2022). Given the typical small size of glassy ejecta samples (e.g., mm to cm scale), it is difficult to evaluate the spatial scale over which the oxidation-fractionation process operates, as well as what process(es) control the efficiency of mechanical separation of the Ni-rich spherules from glass during ejection.

5. Conclusions

We report new compositional data for glassy impactite from the Henbury crater field in Australia. Multiple geochemical proxies (Fe-Si, Ni-Co, Cr-Ir, PGE) indicate that Henbury glass contains on average ~ 10 % projectile contamination by the Henbury IIIAB iron meteorite, although the glass is compositionally heterogenous at μm-scale. The detection of high PGE abundances in Henbury glass is also attributed to projectile contamination. The Henbury glass sample described here is proposed to represent an example of a near primary (least fractionated

meteoritic component) projectile-targe interface melt from a small (<1 km) impact crater. Comparison of textural and geochemical characteristics reveal that Wabar and Kamil glasses represent progressively more evolved interface melts (more fractionated meteoritic components). In addition to projectile components in Henbury glass, we also report the first occurrence of shocked quartz, which provides new evidence of hypervelocity processes from the Henbury crater field.

Data Availability

Data are available through AusGeochem at https://doi.org/10.580 24/AGCUE17519F2.

CRediT authorship contribution statement

Aaron J. Cavosie: Writing – review & editing, Writing – original draft, Project administration, Methodology, Investigation, Formal analysis, Data curation, Conceptualization. **Phil A. Bland:** Writing – review & editing, Resources, Funding acquisition. **Noreen J. Evans:** Writing – review & editing, Validation, Resources, Methodology, Formal analysis. **Kai Rankenburg:** Writing – review & editing, Methodology, Formal analysis. **Malcolm P. Roberts:** Writing – review & editing, Methodology, Formal analysis. **Luigi Folco:** Writing – review & editing, Methodology, Investigation, Formal analysis.

Declaration of competing interest

The authors declare that they have no known competing financial interests or personal relationships that could have appeared to influence the work reported in this paper.
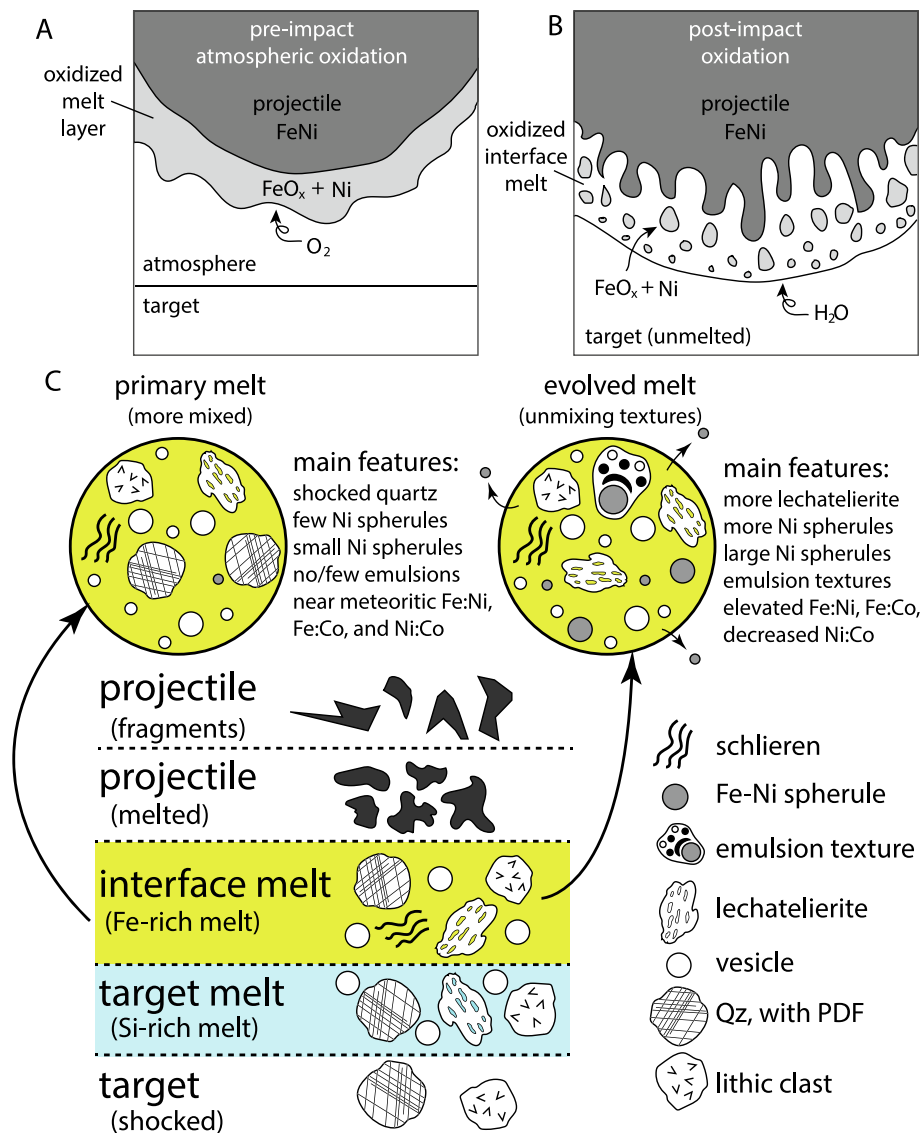
Fig. 13. Model for origin of different features found in melt (glass) from the projectile-target interface formed by collision of an iron meteorite projectile and a silica-rich target rock. (A) Cartoon showing pre-impact oxidation of projectile Fe in the atmosphere. (B) Cartoon showing post-impact oxidation of projectile Fe within impact glass. (C) Interface 'stratigraphy' at the end of the contact/compression stage, when melt forms at the projectile-target interface. The concept of a 'primary' interface melt is one that does not record evidence of widespread unmixing processes (e.g., phase separation) prior to quenching, and where near-meteoritic Fe:Ni, Fe:Co, and Ni:Co ratios are preserved. The concept of an 'evolved' interface melt is one where textures indicative of phase separation processes (e.g., emulsion textures, Ni-rich spherules) are more widely developed, and where siderophile element ratios are fractionated from meteoritic values.

Acknowledgements

Appendix A. Supplementary material

Information on details of the element and ratio mixing model calculations. Figure S1 shoes Henbury glass PGE element-ratio data plots that were used to evaluate if projectile PGE ratios are preserved in Henbury glass.

Supplementary material to this article can be found online at htt ps://doi.org/10.1016/j.gca.2024.02.016.

References

Alderman, A.R., 1932. The meteorite craters at Henbury, Central Australia. Mineral Mag. J. m. Soc. 136, 19–32.

Alvarez, L.W., Alvarez, W., Asaro, F., Michel, H.V., 1980. Extraterrestrial cause for the cretaceous-tertiary extinction. Science 208 (4448), 1095–1108.

Attrep Jr., M., Orth, C.J., Quintana, L.R., 1991. Chemical fractionation of siderophile elements in impactites from australian meteorite craters. In: 22nd Annual Lunar and Planetary Science Conference, pp. 39–40.

Badyukov, D.D., Raitala, 2012. Ablation spherules in the sikhote alin meteorite and their genesis. Petrol. 20 (6), 520–528.

Brett, R., 1967. Metallic spherules in impactite and tektite glasses. Am. Mineral. 52 (5–6), 721–733.

Buchwald, V.F., 1975. Handbook of Iron Meteorites volume 2, 638–644.

Buhl, S., McColl, D., 2015. Henbury craters and meteorites: their discovery. Springer, History and Study.

Chen, J., Mallmann, G., Zhukova, I., O'Neill, H., 2020. Development of PGE-bearing silicate glass standards for quantitative trace element analysis in silicate-based metallurgical slags. J. Sustain. Metal. 6, 691–699.

Cook, P.J., 1968. Explanatory notes on the Henbury geological sheet. Austr. Bur. Min. Res. 19, p.

Dence, M.R., Von Engelhardt, W., Plant, A.G., Walter, L.S., 1974. Indications of fluid immiscibility in glass from West Clearwater Lake impact crater, Quebec. Canada. Contrib. Miner. Petrol. 46, 81–97.

Ding, Y., Veblen, D.R., 2004. Impactite from Henbury. Australia. Am. Mineral. 89 (7), 961–968.

Ebert, M., Hecht, L., Deutsch, A., Kenkmann, T., 2013. Chemical modification of projectile residues and target material in a MEMIN cratering experiment. Meteorit. Planet. Sci. 48, 134–149.

Ebert, M., Hecht, L., Deutsch, A., Kenkmann, T., Wirth, R., Berndt, J., 2014. Geochemical processes between steel projectiles and silica-rich targets in hypervelocity impact experiments. Geochim. Cosmochim. Acta 133, 257–279.

El Goresy, A., 1968. The opaque minerals in impactite glasses. in shock metamorphism of natural materials. Mono Book Corp, pp. 531–553.

Evans, N.J., Gregoire, D.C., Grieve, R.A.F., Goodfellow, W.D., Veizer, J., 1993. Use of platinum-group elements for impactor identification: terrestrial impact craters and cretaceous-tertiary boundary. Geochim. Cosmochim. Acta 57, 3737–3748.

Fazio, A., D'Orazio, M., Cordier, C., Folco, L., 2016. Target-projectile interaction during impact melting at Kamil crater. Egypt. Geochim. Cosmochim. Acta 180, 33–50.

Folco, L., D'Orazio, M., Fazio, A., Cordier, C., Zeoli, A., Ginneken, M.V., El-Barkooky, A., 2015. Microscopic impactor debris in the soil around Kamil crater (Egypt): Inventory, distribution, total mass, and implications for the impact scenario. Meteorit. Planet. Sci. 50, 382–400.

Folco, L., Carone, L., D'Orazio, M., Cordier, C., Suttle, M.D., van Ginneken, M., Masotta, M., 2022. Microscopic impactor debris at Kamil crater (Egypt): the origin of the Fe-Ni oxide spherules. Geochim. Cosmochim. Acta 335, 297–322.

French, B.M., Koeberl, C., 2010. The convincing identification of terrestrial meteorite impact structures: what works, what doesn't, and why. Earth-Sci. Rev. 98 (1–2), 123–170.

Gao, S., Liu, X., Yuan, H., Hattendorf, B., Günther, D., Chen, L., Hu, S., 2002. Determination of forty two major and trace elements in USGS and NIST SRM glasses by laser ablation- inductively coupled plasma-mass spectrometry. Geostand. Res. 26, 181–196.

Gemelli, M., D'Orazio, M., Folco, L., 2015. Chemical analysis of iron meteorites using a hand-held X-ray fluorescence spectrometer. Geostand. Geoanal. Res. 39, 55–69.

Gibbons, R.V., Hörz, F., Thompson, T.D., Brownlee, D.E., 1976. Metal spherules in Wabar, Monturaqui, and Henbury impactites. In Lunar and Planetary Science Conference Proceedings 7, 863–880.

Goderis, S., Paquay, F., Claeys, P., Osinski, G., Pierazzo, E., 2013. Projectile identification in terrestrial impact structures and ejecta material. Impact Cratering: Processes and Products: New York, Wiley-Blackwell 223–239.

Grieve, R.A.F., Palme, H., Plant, A.G., 1980. Siderophile-rich particles in the melt rocks at the E. Clearwater impact structure, Quebec: their characteristics and relationship to the impacting body. Contrib. Miner. Petrol. 75 (3), 187–198.

Hamacher, D.W., Goldsmith, J., 2013. Aboriginal oral traditions of Australian impact craters. J Astron Hist. Herit. 16, 295–311.

Hamann, C., Hecht, L., Ebert, M., Wirth, R., 2013. Chemical projectile–target interaction and liquid immiscibility in impact glass from the Wabar craters. Saudi Arabia. Geochim. Cosmochim. Acta 121, 291–310.

Hamann, C., Fazio, A., Ebert, M., Hecht, L., Wirth, R., Folco, L., Deutsch, A., Reimold, W. U., 2018. Silicate liquid immiscibility in impact melts. Meteorit. Planet. Sci. 53, 1594–1632.

Hezel, D., 2020. MetBase.org as a research and learning tool for cosmochemistry. Elements 16 (1), 73–75.

Hodge, P.W., Wright, F.W., 1971. Meteoritic particles in the soil surrounding the Henbury meteorite craters. J. Geophys. Res. 76 (17), 3880–3895.

Holdship, P., Bonnand, P., Price, D., Watson, D., 2018. Micro flow injection ICP-MS analysis of high matrix samples: an investigation of its capability to measure trace elements in iron meteorites. J. Anal. Atom. Spectrom. 33 (11), 1941–1953.

Hopper, V.D., Sewell, D.K.B., Aitken, D.K., 1990. Study of melt produced bodies observed at Henbury crater region. Int. J. Impact Eng. 10, 251–260.

Hörz, F., See, T.H., Murali, A.V., Blanchard, D.P., 1989. Heterogeneous dissemination of projectile materials in the impact melts from Wabar crater, Saudi Arabia. In: Proceedings of the 19th Lunar and Planetary Science Conference. Lunar and Planetary Institute, pp. 697–709.

Irvine, T.N., Baragar, W.R.A., 1971. A guide to the chemical classification of the common volcanic rocks. Can. J. Earth. Sci. 8, 523–548.

Jarosewich, E., Nelen, J.A., Norberg, J.A., 1980. Reference samples for electron microprobe analysis. Geostand. Newslett. 4, 43–47.

Jochum, K.P., Willbold, M., Raczek, I., Stoll, B., Herwig, K., 2005. Chemical characterization of the USGS reference glasses GSA-1G, GSC-1G, GSD-1G, GSE-1G, BCR-2G, BHVO-2G, and BIR-1G using EPMA, ID-TIMS, ID-ICP-MS and LA-ICP-MS. Geostand. Geoanal. Res. 29, 285–302.

Kelly, W.R., Holdsworth, E., Moore, C.B., 1974. The chemical composition of metallic spheroids and metallic particles within impactite from barringer meteorite crater. Arizona. Geochim. Cosmochim. Acta 38 (4), 533–543.

Koeberl, C., 2014. The Geochemistry and Cosmochemistry of Impacts. Treatise on Geochemistry, Planets, asteroids, and comets and the solar system 2, 2nd ed., pp. 73–118

Koeberl, C., Armstrong, R.A., Reimold, U.W., 1997. Morokweng, South Africa: a large impact structure of jurassic-cretaceous boundary age. Geology 25 (8), 731–734.

Koeberl, C., Claeys, P., Hecht, L., McDonald, I., 2012. Geochemistry of impactites. Elements 8 (1), 37–42.

LeBas, M.J., LeMaitre, R.W., Streckeisen, A., Zanettin, B., 1986. A chemical classification of volcanic rocks based on the total alkali-silica diagram. J. Petrol. 27, 745–750.

Lewis, C.F., Moore, C.B., 1971. Chemical analyses of thirty-eight iron meteorites. Meteoritics 6, 195–205.

Magna, T., Žák, K., Pack, A., Moynier, F., Mougel, B., Peters, S., Skála, R., Jonášová, S., Mizera, J., Řanda, Z., 2017. Zhamanshin astrobleme provides evidence for carbonaceous chondrite and post-impact exchange between ejecta and earth's atmosphere. Nature Communications 8, 227.

MetBase: Meteorite Information Database, http://www.metbase.org, 1994-2023, GeoPlatform UG, Germany.

Milton, D.J., 1968. Structural geology of the Henbury meteorite craters, Northern Territory, Australia. U.S. Geol. Surv. Prof. Paper 599-C, C1–C17.

Mittlefehldt, D.W., See, T.H., Hörz, F., 1992. Dissemination and fractionation of projectile materials in the impact melts from wabar crater. Saudi Arabia. Meteoritics 27 (4), 361–370.

Normington, V.J., Donnellan, N., Thompson, J.M., Meffre, S., 2018. Summary of results. NTGS LA-ICP-MS U-Pb geochronology project: selected samples from the central Amadeus Basin, July 2014-June 2016: Northern Territory Geological Survey, Record 2018-011, 48 pp.

Osinski, G., Grieve, R.A.F., Ferrière, L., Losiak, A., Pickersgill, A.E., Cavosie, A.J., Hibbard, S.M., Hill, P.J.A., Bermudez, J.J., Marion, C.L., Newman, J.D., Simpson, S. L., 2022. Impact Earth: A review of the terrestrial impact record. Earth-Sci. Rev. 232, 104112.

Paton, C., Hellstrom, J., Paul, B., Woodhead, J., Hergt, J., 2011. Iolite: Freeware for the visualization and processing of mass spectrometric data. J. Anal. At. Spectrom 26, 2508.

Pearce, N.J.G., Perkins, W.T., Westgate, J.A., Gorton, M.P., Jackson, S.E., Neal, C.R., Chenery, S.P., 1997. A compilation of new and published major and trace element data for NIST SRM 610 and NIST SRM 612 glass reference materials. Geostand. Res. 21, 115–144.

Pernicka, E., Wasson, J.T., 1987. Ru, Re, OS, Pt and Au in iron meteorites. Geochim. Cosmochim. Acta 51 (6), 1717–1726.

Petaev, M.I., Jacobsen, S.B., 2004. Differentiation of metal-rich meteoritic parent bodies: I. measurements of PGEs, Re, Mo, W, and Au in meteoritic Fe-Ni metal. Meteorit. Planet. Sci. 39 (10), 1685–1697.

Pouchou, J.L., Pichoir, F., 1991. Quantitative analysis of homogeneous or stratified microvolumes applying the model 'PAP'. In: Heinrich, K.F.J., Newbury, D.E. (Eds.), Electron Probe Quantification. Plenum Press, New York.

Pratesi, G., Viti, C., Cipriani, C., Mellini, M., 2002. Silicate-silicate liquid immiscibility and graphite ribbons in Libyan desert glass. Geochim. Cosmochim. Acta 66 (5), 903–911.

Quintero, R.R., Cavosie, A.J., Cox, M.A., Miljković, K., Dugdale, A., 2021. Australian impact cratering record: Updates and recent discoveries. In: Reimold, W.U., Koeberl, C. (Eds.), Large Meteorite Impacts and Planetary Evolution VI. Geol. Soc. Am. Spec. Pap. 550, pp. 41–68.

Rehkämper, M., Halliday, A.N., Fitton, J.G., Lee, D.C., Wieneke, M., Arndt, N.T., 1999. Ir, Ru, Pt, and Pd in basalts and komatiites: new constraints for the geochemical behavior of the platinum-group elements in the mantle. Geochim. Cosmochim. Acta 63 (22), 3915–3934.

Smales, A.A., Mapper, D., Fouché, K.F., 1967. The distribution of some trace elements in iron meteorites, as determined by neutron activation. Geochim. Cosmochim. Acta 31 (5), 673–720.

Spencer, L.J., 1933. Meteoric iron and silica-glass from the meteorite craters of Henbury (Central Australia) and Wabar (Arabia). Miner. Mag. 142, 387–412.

Tagle, R., Hecht, L., 2006. Geochemical identification of projectiles in impact rocks. Meteorit. Planet. Sci. 41 (11), 1721–1735.

Taylor, S.R., 1966. Australites, Henbury impact glass and subgreywacke: a comparison of the abundances of 51 elements. Geochim. Cosmochim. Acta 30, 1121–1136.

Taylor, S.R., 1967. Composition of meteorite impact glass across the Henbury strewnfield. Geochim. Cosmochim. Acta 31, 961–968.

Taylor, S.R., Kolbe, P., 1964. Henbury impact glass: parent material and behaviour of volatile elements during melting. Nature 203, 390–391.

Taylor, S.R., Kolbe, P., 1965. Geochemistry of Henbury impact glass. Geochim. Cosmochim. Acta 29, 741–745.

Taylor, S.R., McLennan, S.M., 1979. Chemical relationships among irghizites, zhamanshinites, Australasian tektites and Henbury impact glass. Geochim. Cosmochim. Acta 43, 1551–1565.

Taylor, S.R., McLennan, S.M., 1995. The geochemical evolution of the continental crust. Rev. Geophys. 33 (2), 241–265.

van Achterbergh, E., Ryan, C.G., Jackson, S.E., Griffin, W.L., 2001. Data reduction software for LA-ICP-MS: appendix. In: Sylvester, P. J. (Ed.), Laser Ablation –ICP-Mass Spectrometry in the Earth Sciences: Principles and Applications. Mineralogical Association of Canada Short Course Series, Ottawa, Ontario, Canada, pp. 239–243, 29.

Wasson, J.T., 1967. Differences of composition among Australian iron meteorites. Nature 216 (5118), 880.

Wasson, J.T., Kallemeyn, G.W., 1988. Compositions of chondrites. Phil. Trans. Roy. Soc. London. Series A, Math. Phys. Sci. 325(1587), 535-544.

Wasson, J.T., Choi, B.-G., Jerde, E.A., Ulff-Moller, F., 1998. Chemical classification of iron meteorites: XII. New members of the magmatic groups. Geochim. Cosmochim. Acta 62, 715–724.

Zolensky, M.E., Koeberl, C., 1991. Why are blue zhamanshinites blue? Liquid immiscibility in an impact melt. Geochim. Cosmochim. Acta 55 (5), 1483–1486.